Journal of Computational Physics **183,** 274–306 (2002)
doi:10.1006/jcph.2002.7197

Computing Three-Dimensional Thin Film Flows Including Contact Lines

Javier A. Diez* and L. Kondic†

**Instituto de Fisica Arroyo Seco, Universidad Nacional del Centro, Pinto 399, 7000, Tandil, Argentina; and*
†Department of Mathematical Sciences, New Jersey Institute of Technology, Newark, New Jersey 07102
E-mail: jdiez@exa.unicen.edu.ar, kondic@pattern.njit.edu

Received April 15, 2002; revised August 13, 2002

We present a computational method for quasi 3D unsteady flows of thin liquid films on a solid substrate. This method includes surface tension as well as gravity forces in order to model realistically the spreading on an arbitrarily inclined substrate. The method uses a positivity preserving scheme to avoid possible negative values of the fluid thickness near the fronts. The "contact line paradox," i.e., the infinite stress at the contact line, is avoided by using the precursor film model which also allows for approaching problems that involve topological changes. After validating the numerical code on problems for which the analytical solutions are known, we present results of fully nonlinear time-dependent simulations of merging liquid drops using both uniform and nonuniform computational grids. © 2002 Elsevier Science (USA)

Key Words: thin film flows; nonlinear fourth-order diffusion; finite differences; drops coalescence; nonuniform grid.

1. INTRODUCTION

The scenario where a solid surface is being coated by a thin liquid film is ubiquitous in nature, and it also appears in a variety of technological problems (microchip production or microscopic fluidic devices). Basically, the coating process develops as a balance between viscous and surface tension forces; in some configurations, other body forces (such as centrifugal [1, 2] or thermocapillary forces [3–5]) may also be relevant to drive the flow. Coating flows exhibit two main features: one is the existence of a free surface, whose position must be calculated as a consequence of the balance among the driving forces, and the other is the presence of a contact line, which defines the boundary between the film and the uncoated surface. The combination of these two characteristics may give a place to complex topologies of stable or unstable flows, with nontrivial shapes of the free surface and corrugations of the contact line.

0021-9991/02 $35.00

Coating flows are usually approached within the lubrication approximation which reduces Navier–Stokes equations to a single nonlinear, fourth-order PDE describing time evolution of the free surface $h(x, y, t)$ (see, e.g., review article [6]). The boundary condition for the normal stress at the free surface is of the Laplace–Young type; we also require that the shear stress vanishes there. The boundary conditions at the contact line are more involved, since, at present, knowledge of the relevant physics is still incomplete [7, 8]. In particular, a moving contact line coupled with no-slip boundary conditions at the solid surface leads to a divergence of viscous energy dissipation; this is the so-called "contact line paradox." In this work, we use the precursor film model, which basically assumes that the solid surface is prewetted, to overcome this problem. Previous studies [9] have shown computational advantages of this approach over the alternative approach that relaxes no-slip at the solid–liquid interface. The main conclusion of these studies was that the precursor film model produced equivalent results to slip models, while significantly reducing the computational effort.

We concentrate on the case of completely wetting fluids (for which the precursor film model is applicable) and employ a "global" model that considers the contact line as an integral part of the system. Our method captures the topological transitions of the flow, such as merging or film rupture, as illustrated in Section 7. Another important feature of the presented method is that it is straightforward to include additional driving mechanisms, such as centrifugal, thermocapillary, or van der Waals forces. These forces simply lead to new terms that can be easily added to the basic formulation. We note that there has recently been considerable activity in computing thin film flows including contact line motion in the flow of both completely and partially wetting fluids. These recent works use van der Waals forces [10, 11], slip model [12], or precursor film [13–16]. While most of these works are based on finite differences, some researchers have also developed volume of fluid methods with numerically introduced slip [17] and finite element methods [18].

In this work we present a detailed description of the implementation of our computational method to simulate lubrication flows over planar substrates. In particular, we present validation tests, as well as computations of the coalescence of a linear array of sessile drops. This is quite an interesting problem because it combines two major phenomena, namely, the contact line motion and the coalescence process itself. Both issues have been studied separately as drop spreading [19–21], or as a coalescence of two cylindrical or spherical drops set in contact [22–26]. Here, we use this challenging combined problem as a benchmark for the performance of our computational method. Finally, we discuss the advantages of performing simulations on nonuniform Cartesian grids.

2. BASIC EQUATIONS

The starting point for modeling coating thin film flows are Navier–Stokes equations for an incompressible fluid ($\nabla \cdot \mathbf{u} = 0$)

$$\frac{\partial \mathbf{u}}{\partial t} + (\mathbf{u} \cdot \nabla)\mathbf{u} = -\frac{1}{\rho}\nabla p + \frac{\mu}{\rho}\nabla^2 \mathbf{u} + g \sin\beta \mathbf{i} - g \cos\beta \mathbf{k}, \tag{1}$$

where $\mathbf{u} = (\mathbf{v}, w)$ is the fluid velocity, p is the pressure, ρ is the density, and μ is the viscosity. The vector $\mathbf{v}$ stands for the x and y velocity components in the plane of the substrate, and w stands for the perpendicular component ($\mathbf{i}$, $\mathbf{j}$ are in-plane, and $\mathbf{k}$ is the perpendicular

unit vector). In this work we concentrate on the flows on a horizontal substrate, where the inclination angle $\beta = 0$; however, we keep β in the presentation for generality.

Major simplification of the above equations follows by using the long-wave (lubrication) approximation, which is outlined here (see, e.g., [19] for details). The main assumptions are that (i) the flow has a negligible Reynolds number, $\mathrm{Re} = UL\rho/\mu$, where U is a typical velocity, L is a typical length scale, and (ii) that $w \ll |\mathbf{v}|$, which follows from the incompressibility condition and the requirement that the film is thin; later we will also assume that the gradients of the solution are small. In the limit of vanishing Re, the inertial terms (right-hand side of Eq. (1)) can be safely ignored, leading to

$$\begin{aligned} \nabla_2 p &= \mu \frac{\partial^2 \mathbf{v}}{\partial z^2} + \rho g \sin\beta \mathbf{i}, \\ \frac{\partial p}{\partial z} &= -\rho g \cos\beta, \end{aligned} \tag{2}$$

where $\nabla_2 = (\partial_x, \partial_y)$. Integration of these equations leads to the well-known quadratic velocity profile:

$$\mathbf{v} = \left[\frac{1}{\mu}\nabla_2 P - \frac{\rho g}{\mu}\sin\beta \mathbf{i}\right]\left[\frac{z^2}{2} - hz\right], \tag{3}$$

where $P = \rho g h \cos\beta - \gamma\kappa$, and we use the following boundary conditions: (1) No-slip boundary condition at the solid surface; i.e., $\mathbf{v}|_{z=0} = 0$; (2) Laplace–Young boundary condition at the air/fluid interface, $z = h(x, y)$, $p(h) = -\gamma\kappa + p_0$, where γ is the surface tension, $\kappa \approx \nabla^2 h$ is the curvature, and p_0 is the atmospheric pressure; and (3) vanishing shear stresses at $z = h(x, y)$, leading to $\partial\mathbf{v}/\partial z|_{z=h(x,y)} = 0$. Integration over the short, z, dimension allows us to define the averaged flow velocity $\langle\mathbf{v}\rangle$ as

$$\langle\mathbf{v}\rangle = -\frac{h^2}{3\mu}[\nabla P - \rho g \sin\beta \mathbf{i}]. \tag{4}$$

The continuity equation for a fluid element of volume $h(x, y)\,dx\,dy$ is

$$\frac{\partial h}{\partial t} + \nabla \cdot (h\langle\mathbf{v}\rangle) = 0. \tag{5}$$

Substitution of the expression for $\langle\mathbf{v}\rangle$ from Eq. (4) leads to

$$\frac{\partial h}{\partial t} = -\frac{1}{3\mu}\nabla \cdot [\gamma h^3 \nabla\nabla^2 h - \rho g h^3 \nabla h \cos\beta + \rho g h^3 \sin\beta \mathbf{i}]. \tag{6}$$

Thus, the lubrication approximation reduces Navier–Stokes equations to a nonlinear fourth-order PDE that governs the time evolution of the film thickness $h(x, y, t)$. Choosing the scales h_c, x_c, and t_c for h, x, y, and t, we cast Eq. (6) into the following nondimensional form,

$$\frac{\partial h}{\partial t} = -\mathcal{C}\nabla \cdot [h^3 \nabla\nabla^2 h] + \mathcal{G}\nabla \cdot [h^3 \nabla h] - \mathcal{F}\frac{\partial h^3}{\partial x}, \tag{7}$$

where h, x, y, and t are now *dimensionless* variables. The constants $\mathcal{C}$, $\mathcal{G}$, and $\mathcal{F}$ depend on the scales and will be specified as appropriate for the problem at hand.

As mentioned in the Introduction, all theoretical and computational methods require some regularizing mechanism—either assumption of a thin precursor film in front of the apparent contact line [27–29] or relaxing the no-slip boundary condition at the fluid–solid interface [19, 30, 31]. We have recently performed an extensive analysis of the computational performance of these regularizing mechanisms applied to the spreading drop problem [9]. In that paper it is shown that the precursor film performs much better computationally than the various slip models. Hence, we also use a precursor film of nondimensional thickness b as a regularizing method in this work.

3. SPATIAL DISCRETIZATION

The numerical domain is a rectangle defined by $0 \le x \le L_x$ and $0 \le y \le L_y$, which is divided into $N = n_x \times n_y$ rectangular cells of variable size (see Fig. 1). The cell dimensions, Δx_i and Δy_j, are, in general, arbitrary (smooth) functions of the coordinates of the mesh nodes x_i and y_j, respectively. These are generated by

$$x_{i+1} = x_i + \Delta x_i, \quad y_{j+1} = y_j + \Delta y_j, \tag{8}$$

with $1 \le i \le n_x$, $1 \le j \le n_y$. The code is prepared to work with a user-supplied routine that yields a variable grid considered appropriate for the problem under study; naturally, a uniform grid with constant Δx and Δy is included as a special case. The presented method is second-order accurate subject to the conditions on the nonuniformity of the grid specified at the end of this section.

To simplify the presentation we define the index $k = i + (j-1)n_x$; see Figs. 1 and 2. Spatial discretization of the governing Eq. (7) using central finite differences (described in detail below) then leads to the following system of ODEs

$$\frac{\partial h_k}{\partial t} = -f_k = -\sum_{m=1}^{7} f_k^{(m)}. \tag{9}$$

Here, $h_k(t)$ is the discrete approximation to $h(x, y, t)$ at the center of the kth cell, and f_k is

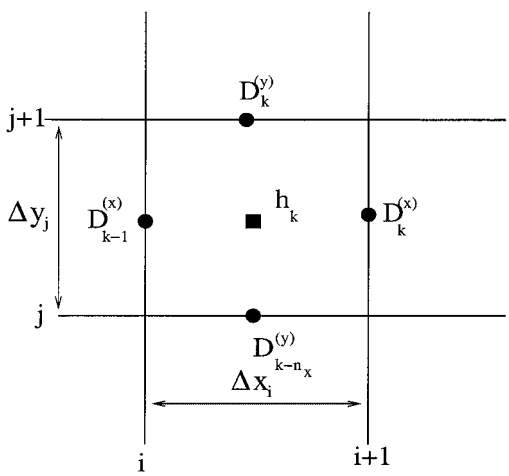

FIG. 1. A typical cell of the mesh.

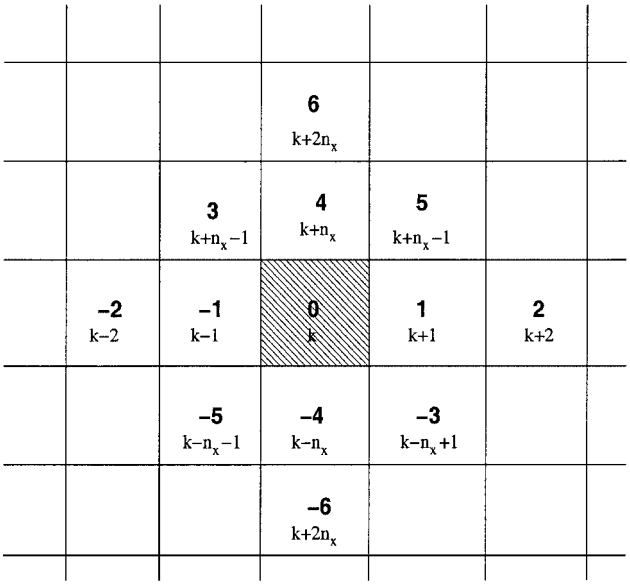

FIG. 2. The shaded kth cell is locally denoted by index 0, and the neighboring cells involved in the finite differences are numbered as shown.

a nonlinear operator which depends on the values of h_k at the neighboring grid points. The discretization of each term on the right-hand side of Eq. (7) (seven terms when expressed in Cartesian coordinates) is denoted by $f_k^{(m)}$. Nonuniformity of the grid leads to rather complex expressions which are presented in Appendix A.

3.1. Surface Tension Term

The first four terms in Eq. (9) ($m = 1, 2, 3, 4$) are due to surface tension force and result from the expansion of the first term on the right-hand side of Eq. (7) as

$$\nabla \cdot [D(h)\nabla\nabla^2 h] = \frac{\partial}{\partial x}\left(D(h)\frac{\partial^3 h}{\partial x^3}\right) + \frac{\partial}{\partial y}\left(D(h)\frac{\partial^3 h}{\partial y^3}\right) + \frac{\partial}{\partial x}\left(D(h)\frac{\partial^3 h}{\partial y^2 \partial x}\right) + \frac{\partial}{\partial y}\left(D(h)\frac{\partial^3 h}{\partial x^2 \partial y}\right), \tag{10}$$

where $D(h) = h^3$ is the nonlinear diffusivity. We present here the expressions for $f_k^{(1)}$ and $f_k^{(3)}$ and indicate how to obtain the corresponding expressions for $f_k^{(2)}$ and $f_k^{(4)}$.

Use of centered finite differences leads to the following expression for $f_k^{(1)}$ that involves five grid points along the horizontal $y = \text{const.}$ line (the points are marked as $-2, -1, 0, 1,$ and 2 in Fig. 2),[1]

$$f_k^{(1)} = a_{-2}^{(1)} h_{k-2} + a_{-1}^{(1)} h_{k-1} + a_0^{(1)} h_k + a_1^{(1)} h_{k+1} + a_2^{(1)} h_{k+2}, \tag{11}$$

[1] The coefficients $a_l^{(m)}$, $L_l^{(m)}$, and similar coefficients are also k-dependent; we omit this index for brevity if there is no possibility for confusion.

where

$$a_l^{(1)} = L_l^{(1)} D_{k-1}^{(x)} + R_l^{(1)} D_k^{(x)}, \quad -2 \le l \le 2, \tag{12}$$

and

$$D_k^{(x)} = \tilde{D}(h_k, h_{k+1}). \tag{13}$$

Here, $\tilde{D}$ stands for an appropriate interpolation of the diffusivity $D(h)$ (see Section 3.2) at the border (grid line) of two consecutive cells in the x direction ($\Delta k = \pm 1$). Thus, $D_{k-1}^{(x)}(D_k^{(x)})$ is evaluated at the left (right) side of the kth cell (see Fig. 1). The coefficients $L_l^{(1)}$ (left) and $R_l^{(1)}$ (right) are, in general, grid-dependent functions, given in Appendix A.

The second term in Eq. (10) is analogous to the first term, with appropriate substitutions (see Fig. 2), yielding

$$f_k^{(2)} = a_{-6}^{(2)} h_{k-2n_x} + a_{-4}^{(2)} h_{k-n_x} + a_0^{(2)} h_k + a_4^{(2)} h_{k+n_x} + a_6^{(2)} h_{k+2n_x}, \tag{14}$$

where

$$a_l^{(2)} = B_l^{(2)} D_{k-n_x}^{(y)} + T_l^{(2)} D_k^{(y)}, \quad l = -6, -4, 0, 4, 6, \tag{15}$$

and

$$D_k^{(y)} = \tilde{D}\left(h_k, h_{k+n_x}\right). \tag{16}$$

The coefficients $B_l^{(2)}$ (bottom) and $T_l^{(2)}$ (top) are obtained by exchanging $\Delta x_i \to \Delta y_j$ in the expressions for $L_l^{(1)}$ and $R_l^{(1)}$ (Appendix A). Also, $D_{k-n_x}^{(y)}(D_k^{(y)})$ are evaluated at the middle of the bottom (top) side of the kth cell.

The cross derivatives in the third term of Eq. (10) include nine neighboring cells (marked as ± 5, ± 4, ± 3, ± 1, and 0 in Fig. 2), giving

$$\begin{aligned} f_k^{(3)} = {} & a_{-5}^{(3)} h_{k-n_x-1} + a_{-4}^{(3)} h_{k-n_x} + a_{-3}^{(3)} h_{k-n_x+1} + a_{-1}^{(3)} h_{k-1} + a_0^{(3)} h_k + a_1^{(3)} h_{k+1} \\ & + a_3^{(3)} h_{k+n_x-1} + a_4^{(3)} h_{k+n_x} + a_5^{(3)} h_{k+n_x+1}, \end{aligned} \tag{17}$$

where

$$a_l^{(3)} = L_l^{(3)} D_{k-1}^{(x)} + R_l^{(3)} D_k^{(x)}, \quad l = \pm 5, \pm 4, \pm 3, \pm 1, 0. \tag{18}$$

Finally, the fourth term in Eq. (10) yields

$$\begin{aligned} f_k^{(4)} = {} & a_{-5}^{(4)} h_{k-n_x-1} + a_{-4}^{(4)} h_{k-n_x} + a_{-3}^{(4)} h_{k-n_x+1} + a_{-1}^{(4)} h_{k-1} + a_0^{(4)} h_k + a_1^{(4)} h_{k+1} \\ & + a_3^{(4)} h_{k+n_x-1} + a_4^{(4)} h_{k+n_x} + a_5^{(4)} h_{k+n_x+1}, \end{aligned} \tag{19}$$

where

$$a_l^{(4)} = B_l^{(4)} D_{k-n_x}^{(y)} + T_l^{(4)} D_k^{(y)}, \quad l = \pm 5, \pm 4, \pm 3, \pm 1, 0. \tag{20}$$

Similarly, as above, the coefficients $B_l^{(4)}$ and $T_l^{(4)}$ are obtained by exchanging $\Delta x_i \leftrightarrow \Delta y_j$ in the expressions for $L_l^{(3)}$ and $R_l^{(3)}$ (Appendix A).

3.2. Discretization of the Diffusivity

In one-dimensional simulations, we have analyzed the performance of the positivity preserving scheme (PPS) [32, 33] to discretize the diffusivity $D(h) = h^s (s \geq 1)$ in Eq. (10) [9]. In those simulations, we have found that this scheme allows for computations on coarser grids. This property is of capital importance for the computationally expensive 2D (or quasi 3D) simulations presented here.

In a 1D setting, PPS prescribes the following interpolation of the diffusivity at the node i (h_i is defined at the center of the line element (x_i, x_{i+1}))

$$D_i = \begin{cases} \frac{h_{i+1} - h_i}{g_{i+1} - g_i}, & h_{i+1} \neq h_i \\ h_i^s, & h_{i+1} = h_i \end{cases}, \tag{21}$$

where

$$g(h) = \int \frac{dh}{D(h)} = \begin{cases} h^{1-s}/(1-s), & s \neq 1 \\ \ln h, & s = 1 \end{cases}. \tag{22}$$

For our 2D problem with $s = 3$, this interpolation leads to the following expression for $\tilde{D}$ in Eqs. (13) and (16), for $h_k \neq h_{k+1}$

$$D_k^{(x)} = 2\frac{h_k^2 h_{k+1}^2}{h_k + h_{k+1}}, \quad D_k^{(y)} = 2\frac{h_k^2 h_{k+n_x}^2}{h_k + h_{k+n_x}}. \tag{23}$$

For $0 < s < 2$, the above-mentioned technique does not guarantee positive values of h_k. However, a positive smooth solution can be guaranteed for the regularized problem [34]. The regularization involves altering the definition of $D(h)$ and also lifting the initial condition $h(x, 0)$ by an amount b (artificial precursor film). The regularized new diffusivity is of the form [35]

$$D_{reg}(h) = \frac{D(h)h^4}{\varepsilon D(h) + h^4}, \tag{24}$$

where $\varepsilon = \varepsilon(b)$ is a small parameter. Note that $D_{reg}(h) \to D(h)$ as $\varepsilon \to 0$, and also that $D_{reg}(h) \to h^4/\varepsilon$ for $h \to 0$ and $s < 4$, which is a more tractable singularity. In particular, in the case of planar symmetry it is required [34] that $b < \varepsilon^{1/2}$ for $2 < s < 3$ and $b \leq \varepsilon^{2/5}$ for $3/8 < s < 2$. Here, we shall take $b = \varepsilon^{0.3}$ whenever regularization is needed. Thus, ε is defined by

$$\varepsilon = \begin{cases} b^{10/3}; & \text{if } s < 2 \\ 0; & \text{if } s \geq 2. \end{cases} \tag{25}$$

We use this scheme to simulate cases with $s = 1$, whose analytical solutions are known (see Section 6).

3.3. Gravity Terms

In this section we present the discretization developed for the (second-order) gravity terms. Usually, the performance of a scheme is determined by the discretization of the

highest order term, as long as the order of approximation of the lower order terms is at least the same as that of the high-order term. For the particular problems considered in this paper, it is, however, important that this discretization preserves the conservative properties of the continuous equation.

3.3.1. *Normal Component of Gravity*

The normal gravity term (third term on the right-hand side of Eq. (7)) in Cartesian coordinates reads as

$$\nabla \cdot [G(h)\nabla h] = \frac{\partial}{\partial x}\left(G(h)\frac{\partial h}{\partial x}\right) + \frac{\partial}{\partial y}\left(G(h)\frac{\partial h}{\partial y}\right), \tag{26}$$

where $G(h) = h^3$. It is discretized using centered finite difference as

$$G_k^{(x)} = \frac{h_k^3 + h_{k+1}^3}{2}, \quad G_k^{(y)} = \frac{h_k^3 + h_{k+n_x}^3}{2}. \tag{27}$$

Thus, the discretization of the first term in Eq. (26) takes the form (see Fig. 2),

$$f_k^{(5)} = a_{-1}^{(5)} h_{k-1} + a_0^{(5)} h_k + a_1^{(5)} h_{k+1}, \tag{28}$$

where

$$a_l^{(5)} = L_l^{(5)} G_{k-1}^{(x)} + R_l^{(5)} G_k^{(x)}, \quad l = -1, 0, 1, \tag{29}$$

and $G_k^{(x)}$ is located at the boundaries of the cell similarly to the definition of $D_k^{(x)}$ in Fig. 1.

Analogously, for the second term in Eq. (26), we have

$$f_k^{(6)} = a_{-4}^{(6)} h_{k-n_x} + a_0^{(6)} h_k + a_4^{(6)} h_{k+n_x}, \tag{30}$$

where

$$a_l^{(6)} = B_l^{(6)} G_{k-n_x}^{(y)} + T_l^{(6)} G_k^{(y)}, \quad l = -4, 0, 4. \tag{31}$$

The general expressions for $L_l^{(5)}$, $R_l^{(5)}$, $B_l^{(6)}$, and $T_l^{(6)}$ for a nonuniform grid are given in Appendix A.

3.3.2. *Parallel Component of Gravity*

The fourth term on the right-hand side of Eq. (7) is discretized as

$$\left(\frac{\partial h^3}{\partial x}\right)_k \approx \frac{1}{4\Delta x_i}\left[\left(h_{k+1}^2 + h_k^2\right)(h_{k+1} + h_k) - \left(h_k^2 + h_{k-1}^2\right)(h_k + h_{k-1})\right], \tag{32}$$

so that we have

$$f_k^{(7)} = a_{-1}^{(7)} h_{k-1} + a_0^{(7)} h_k + a_1^{(7)} h_{k+1}, \tag{33}$$

where

$$a_l^{(7)} = L_l^{(7)} H_{k-1} + R_l^{(7)} H_k, \quad l = -1, 0, 1, \tag{34}$$

and

$$H_k = \frac{h_k^2 + h_{k+1}^2}{2}. \tag{35}$$

3.4. Final Expressions

By summing up the equations for $f_k^{(m)}$ with $m = 1, \ldots, 7$, we obtain (see Eq. (9))

$$\begin{aligned} f_k = {} & a_{k,-6} h_{k-2n_x} + a_{k,-5} h_{k-n_x-1} + a_{k,-4} h_{k-n_x} + a_{k,-3} h_{k-n_x+1} + a_{k,-2} h_{k-2} \\ & + a_{k,-1} h_{k-1} + a_{k,0} h_k + a_{k,1} h_{k+1} + a_{k,2} h_{k+2} + a_{k,3} h_{k+n_x-1} \\ & + a_{k,4} h_{k+n_x} + a_{k,5} h_{k+n_x+1} + a_{k,6} h_{k+2n_x}, \end{aligned}$$

where

$$\begin{aligned} a_{k,l} = {} & L_{k,l} D_{k-1}^{(x)} + R_{k,l} D_k^{(x)} + B_{k,l} D_{k-n_x}^{(y)} + T_{k,l} D_k^{(y)} + \hat{L}_{k,l} G_{k-1}^{(x)} + \hat{R}_{k,l} G_k^{(x)} \\ & + \hat{B}_{k,l} G_{k-n_x}^{(y)} + \hat{T}_{k,l} G_k^{(y)} + \tilde{L}_{k,l} H_{k-1} + \tilde{R}_{k,l} H_k, \end{aligned} \tag{36}$$

and

$$\begin{aligned} L_{k,l} &= \mathcal{C} \sum_{m=1}^{4} L_l^{(m)}, \quad R_{k,l} = \mathcal{C} \sum_{m=1}^{4} R_l^{(m)}, \\ B_{k,l} &= \mathcal{C} \sum_{m=1}^{4} B_l^{(m)}, \quad T_{k,l} = \mathcal{C} \sum_{m=1}^{4} T_l^{(m)}, \\ \hat{L}_{k,l} &= \mathcal{G} \sum_{m=5}^{6} L_l^{(m)}, \quad \hat{R}_{k,l} = \mathcal{G} \sum_{m=5}^{6} R_l^{(m)}, \\ \hat{B}_{k,l} &= \mathcal{G} \sum_{m=5}^{6} B_l^{(m)}, \quad \hat{T}_{k,l} = \mathcal{G} \sum_{m=5}^{6} T_l^{(m)}, \\ \tilde{L}_{k,l} &= \mathcal{F} L_l^{(7)}, \quad \tilde{R}_{k,l} = \mathcal{F} R_l^{(7)}. \end{aligned} \tag{37}$$

In summary, the nonlinear operator f_k is a combination of the 13 values h_k in the neighboring cells, with coefficients $a_{k,l}$. These coefficients contain the nonlinear contributions (D's, G's, or H's) of each (discretized) term of Eq. (7) at the four boundaries of the kth cell (see Eq. (36)). The weight of each contribution depends on the finite differences expression of the corresponding term on the (uniform or nonuniform) grid (see Eq. (37)).

We note that the implementation of the resulting scheme is robust and versatile. First, the addition of other physical effects is achieved very easily by simply adding extra terms to the definition of $a_{k,l}$; see Eq. (36). Second, various boundary conditions can be simply implemented by modifying directly the coefficients of Eq. (37). Since these conditions usually involve only h and its derivatives, and are not time-dependent, the coefficients in Eq. (37) are determined only at the beginning of the calculation. This approach saves

computing time, as well as effectively reduces the effort of computing on a nonuniform grid to that on a uniform grid with the same number of cells.

The discretization outlined in this section is clearly second-order accurate when applied on a uniform grid. Grid nonuniformity can in principle lead to a decrease in the order of accuracy. To analyze this effect, consider for a moment a simple example of the central difference formula applied to calculate the first derivative in the x direction at the point k. To simplify the notation, let $j = 1$, so that $i = k$ (see also Fig. 2). Simple error analysis (performed in a standard manner using Taylor series expansion) shows that the truncation error on a nonuniform grid (using the notation as in Fig. 1) is of the order $(\Delta x_{i+1} - \Delta x_{i-1}) + O(\Delta x_i^2)$. Therefore, if our grid is weakly nonuniform, in the sense that $1 - \Delta x_{i-1}/\Delta x_{i+1} = O(\Delta x_i)$, then the second-order accuracy is preserved. The grids used in this work satisfy this property; more details regarding second-order accuracy are given in the following, in particular in Section 7.

4. BOUNDARY CONDITIONS

In this work we concentrate on the problems characterized by no-flow boundary conditions of Neumann type. As mentioned above, our computational method allows for easy modification of the boundary conditions.

No-flow boundary conditions are implemented by setting to zero the normal component of $\mathbf{\Phi}$ on all sides of the domain, where $\mathbf{\Phi} = h\mathbf{v}$ is the fluid flux, and $\mathbf{v}$ is the dimensionless version of the velocity in Eq. (4). For instance, along the line $y = 0$ $(0 \le x \le L_x)$, we set $\mathbf{\Phi}_y = 0$ by requiring that

$$\frac{\partial h}{\partial y} = \frac{\partial^3 h}{\partial y^3} = 0, \quad \text{at } y = 0, \quad 0 \le x \le L_x. \tag{38}$$

To enforce this condition, we need two fictitious rows of cells outside the domain, that are mirror images of two interior adjacent cells. Thus, for the first and second rows below the x axis ($j = 0$) we have the mirror conditions $h_{k-n_x} = h_k$, $h_{k-2n_x} = h_{k+n_x}$, $1 \le k \le n_x$. Proceeding analogously with the other three sides, we define a rectangular frame (two-cell width) surrounding the real domain. Care is required if the parallel gravity term enters the problem, since the normal component of the velocity along $x = 0$, L_x boundaries contains an additional term proportional to h^2. To have a vanishing flow there, we enforce $h = 0$ whenever this term has to be calculated in the fictitious cells, thus ensuring volume conservation.

The boundary conditions affect the evaluation of Eq. (36) at k's for which some of the 13 neighbors fall outside the physical domain (note that some cells near the corners include mirror "reflections" on two sides). The values of the (grid-dependent) coefficients $L_{l,k}, \ldots, \hat{L}_{l,k}, \ldots, \tilde{L}_{l,k}$ (Eq. (37)) for such cells are redefined using the appropriate fictitious cells. Also, the solution-dependent coefficients ($D_k^{(x)}$, $G_k^{(x)}$, H_k, etc.) in the fictitious cells are defined using the mirror values of h. We note that this assignment has to be made only at the beginning of the calculation.

The no-flow boundary conditions considered here assure us that the fluid volume V within the physical domain remains constant in time; i.e.,

$$V = \int_0^{L_x} \int_0^{L_y} h(x, y, t)\, dx\, dy \cong \sum_{i=1}^{n_x} \sum_{j=1}^{n_y} h_k^n\, \Delta x_i \Delta y_j = \text{const.}, \tag{39}$$

where n indicates the nth time level. The constancy of V during the evolution constitutes an excellent check of the accuracy of the solution. All presented simulations preserve V with a relative error less than 10^{-11}. It should be pointed out that since only the normal component of the velocity is set to zero and the tangential component is set free, the boundaries of the domain may represent "slipping walls" as well as symmetry planes. We will see that this feature is very useful to study flows characterized by some degree of symmetry.

5. TIME DISCRETIZATION

The time discretization of Eqs. (9), $1 \le k \le N$ is performed by Θ-scheme

$$\frac{h_k^{n+1} - h_k^n}{\Delta t^n} + \theta f_k^{n+1} + (1-\theta)\, f_k^n = 0, \tag{40}$$

where $0 \le \theta \le 1$ and n stands for the time level t^n. Here, $\theta = 0$ gives the forward Euler scheme (explicit, $O(\Delta t^n)$), $\theta = 1$ gives the backward Euler scheme (implicit, $O(\Delta t^n)$), and $\theta = 1/2$ yields the Crank–Nicholson scheme (implicit, $O((\Delta t^n)^2)$).

Equation (40) forms a system of N nonlinear algebraic equations, which are solved using iterative Newton–Kantorovich's method. Briefly, the solution at time t^{n+1} is written as

$$h_k^{n+1} = h_k^* + q_k, \tag{41}$$

where h_k^* is a guess and q_k is the correction. To linearize the equations, we expand in Taylor series around h_k^*

$$f_k^{n+1} = f_k^* + \left.\frac{\partial f_k}{\partial q_l}\right|^* q_l, \tag{42}$$

so that Eq. (40) becomes

$$(\delta_{k,l} + \theta \Delta t^n F_{k,l}^*) q_l = R_k, \tag{43}$$

where $\delta_{k,l}$ is the Kronecker delta, and

$$F_{k,l}^* = \left.\frac{\partial f_k}{\partial q_l}\right|^* \tag{44}$$

is the Jacobian matrix (the asterisk indicates evaluation using the guess h_k^*). Each row of this matrix has at most 13 nonzero elements, which are given in Appendix B. The natural ordering of the grid points that we use in this work results in this matrix being in a usual block diagonal form.

The right-hand side in Eq. (43) is given by

$$R_k = h_k^n - h_k^* - \theta \Delta t^n f_k^* - (1-\theta)\Delta t^n f_k^n. \tag{45}$$

The linear system specified by Eq. (43) is then solved for the correction q_k using the biconjugate gradient method. Concerning the guess for the solution, we usually use $h_k^* = h_k^n$, i.e., the solution at the previous time level. If $Q = \max_k(q_k)$, $1 \le k \le N$, is greater than a given tolerance (typically, we choose 10^{-10}), then $h_k^* + q_k$ is taken as a new guess. This

procedure is iteratively performed until Q is less than the tolerance. In Section 7.1, we provide more details regarding the number of iterations needed for convergence of both biconjugate gradient and Newton iterations in the case of the coalescence of two sessile drops.

5.1. Time Step Control

In this work, we use $\theta = 1/2$, which leads to an unconditionally stable scheme. However, one still needs to consider a number of issues when deciding on the size of the time step. The most obvious requirement is to produce an accurate result; this is explained in more detail below. Another requirement is that the solution has to be strictly positive; too large of a time step may let the solution erroneously approach zero. The final aspect that influences the size of the time step is the fact that the guess for the solution may not be close enough to the correct solution. This may prevent the Newton method outlined above from converging in a reasonable number of iterations and augment computational time unnecessarily. Obviously, there is an optimum value of the time step which is, in our simulations, determined dynamically using these three criteria.

The accuracy requirement for the Crank-Nicholson scheme is formulated as follows. Since the scheme is $O(\Delta t^2)$, the relative error of the numerical solution at the point k is given by

$$E_k = \frac{(\Delta t^n)^2}{h_k^n} \left| \frac{d^2 h_k^n}{dt^2} \right|. \tag{46}$$

By multiplying the expansions around h_k^n and h_k^{n-1} by Δt^{n-1} and Δt^n (time steps performed before and after t^n), respectively, and summing up we obtain the following expression for the maximum relative error:

$$E = \max_{1 \le k \le N} \left[\frac{2\Delta t^n}{\Delta t^{n-1}} \frac{\Delta t^{n-1} h_k^{n+1} + \Delta t^n h_k^{n-1} - (\Delta t^{n-1} + \Delta t^n) h_k^n}{(\Delta t^{n-1} + \Delta t^n) h_k^n} \right]. \tag{47}$$

If E is less than a given tolerance Tol (typically, $\text{Tol} = 10^{-2} - 10^{-3}$), the solution h_k^{n+1} obtained using time step Δt^n is accepted; otherwise, the time step is reduced and a new iteration is performed.

6. CODE VALIDATION

The optimal way of validating a numerical code is to compare its results to a known analytical solution. It is clear that the nonlinear fourth-order term in Eq. (7) is the most critical feature of the computation; therefore we must look for a problem involving this high-order term. Since there are no analytical solutions for problems involving surface tension with contact lines ($s = 3$), we test the code using $s = 1$. The analytic solutions for this value of s are of source-type, emulating the "spreading" of a drop. First we test the correctness and convergence properties of our code assuming radial symmetry [36], and then using elliptical symmetry [37].

6.1. Radial Spreading with $s = 1$

We consider the special case $\mathcal{C} = 1$ and $\mathcal{G} = \mathcal{F} = 0$ and assume radial symmetry.[2] The solution emulates the "spreading" of a "drop" of constant volume, V, governed by the equation,

$$\frac{\partial h}{\partial t} + \nabla \cdot (h \nabla \nabla^2 h) = 0. \tag{48}$$

By performing a scaling analysis, one obtains the self-similar solution [36]

$$h(r, t) = H_s(t) \left[1 - \left(\frac{r}{r_{f,s}(t)} \right)^2 \right]^2, \tag{49}$$

where

$$r_{f,s}(t) = \left[192 \left(\frac{3V}{\pi} \right) t \right]^{1/6}, \quad H_s(t) = \frac{3V}{\pi (r_{f,s}(t))^2}, \tag{50}$$

are the radius of the front ($h(r_{f,s}(t), t) = 0$) and the thickness at the center of the drop ($r = 0$), respectively. The self-similar solution given by Eqs. (49) and (50) is reached asymptotically for an arbitrary initial condition. It is also the exact solution of the degenerate problem in which the initial condition is given by a delta function $\delta(r)$ (see, e.g., [38]). While we cannot start the simulations using $\delta(r)$, we can use the profile to which $\delta(r)$ would evolve after some specified time, t_0. Therefore, we specify the initial condition

$$h(r, 0) = (1 - x^2 - y^2)^2 \tag{51}$$

and require that $h(r, 0)$ agrees with Eq. (49) for $r_{f,s}(t_0) = H_s(t_0) = 1$. It can be easily checked that this initial condition would be reached by $\delta(r)$ at $t_0 = (\pi/3V)/192$. For any time $t > t_0$, the evolution proceeds according to Eq. (49), with the front position and the thickness at $r = 0$ given by

$$\begin{aligned} r_f(t) &= [1 + t/t_0]^{1/6}, \\ H(t) &= [192 t_0 (1 + t/t_0)]^{-1/3}. \end{aligned} \tag{52}$$

Since in our case $V = \pi/3$, it follows that $t_0 = 1/192$, fully specifying the solution. It should be noted that the computations still require use of a precursor film to avoid a singular Jacobian matrix of the discrete system, Eq. (43).

Figure 3 shows the comparison of numerical and analytical results for the front position, $r_f(t)$. We use $b = 10^{-3}$ on a uniform grid ($\Delta x_i = \Delta y_j = \text{const.}$), and keep constant $\Delta t = 10^{-5}$ small enough, to reduce errors resulting from time discretization. The symmetry of the problem allows for the simulations to be performed in the first quadrant only; therefore we choose the domain $0 \le x \le 3$, $0 \le y \le 3$. The front position $r_f(t)$ is defined as the position of the depression that develops just in front of the main body of the fluid (see [9] and Fig. 8), along the line $y = 0$. Figure 3 shows clearly that the solution

[2] We note that $s = 1$ is not a physical case and we choose $\mathcal{C} = 1$ for illustration only.

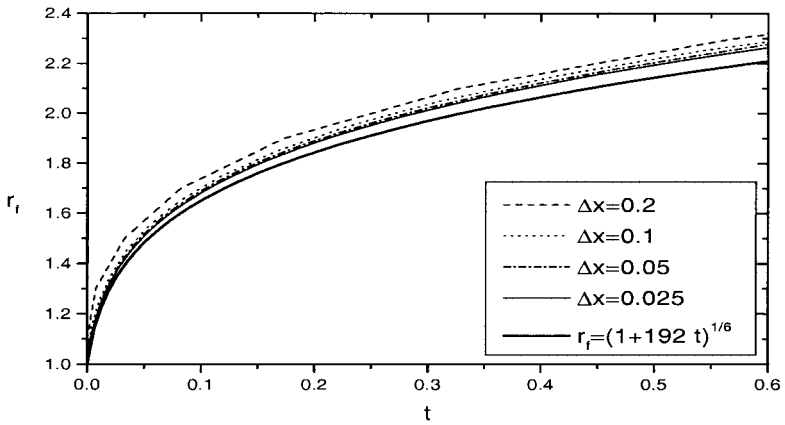

FIG. 3. Time evolution of the front position $x_f(t)$ of the radial drop spreading with $s = 1$ and $b = 10^{-3}$. The thick solid line corresponds to the self-similar solution, Eq. (52).

$r_f(t)$ converges as the cell size decreases. The difference of the computed and the analytical solution given by Eq. (52) (thick solid line) is due to the presence of our artificial precursor film. We have verified that this difference decreases for smaller b's. Naturally, smaller b's also require smaller grid sizes, even when using the regularization scheme specified by Eq. (24). The drop thickness at the center, $H(t)$, converges quadratically to the analytical solution. For instance, $H(t = 0.6)$ takes values 0.2518, 0.2129, 0.2025 for $\Delta x = 0.2, 0.1, 0.05$, respectively. The analytical value is 0.2049, and this value is approached as $b \to 0$.

6.2. Elliptical Spreading

To validate our code using a problem that explicitly involves more than one space dimension, we consider the spreading of an initially ($t = 0$) elliptical drop

$$h(x, y, 0) = H_0\left(1 - \frac{x^2}{a_0} - \frac{y^2}{b_0}\right)^2, \tag{53}$$

where $\sqrt{a_0}$ and $\sqrt{b_0}$ are lengths of the semi-axes. For the case $s = 1$, we assume that for $t > 0$

$$h(x, y, t) = H(t)\left(1 - \frac{x^2}{a(t)} - \frac{y^2}{b(t)}\right)^2, \tag{54}$$

where $a(t), b(t)$, and $H(t)$ are obtained by substituting this ansatz into Eq. (48). The solution is given implicitly in terms of the difference $\alpha(t) = a(t) - b(t)$ as [37]

$$2^9\sqrt{\Sigma}(t + t_1) = -\beta \tanh^{-1}\sqrt{1 - \alpha^6/\beta^2} + \frac{\sqrt{\beta^2 - \alpha^6}}{3\alpha^6}(\beta^2 + 2\alpha^6), \tag{55}$$

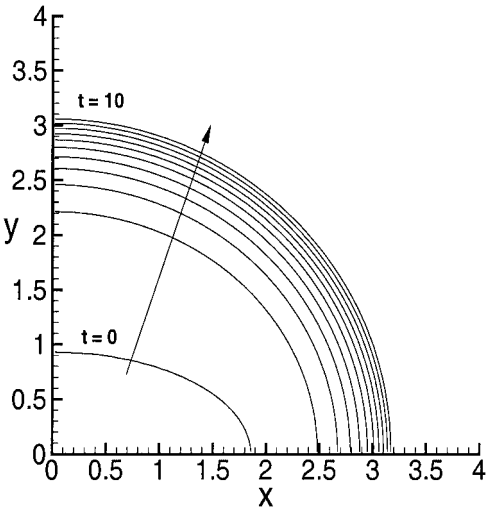

FIG. 4. Time evolution of the shape of the contact line for spreading of an elliptical drop with $s = 1$, $b = 10^{-3}$, $a_0 = 4$, and $b_0 = 1$. The time interval between consecutive curves is $\delta t = 1$. These results are obtained using $\Delta x = \Delta y = 0.05$.

where

$$\Sigma = H(t)^2 a(t) b(t) = \left(\frac{45}{52} V\right)^2 = \text{const.}, \tag{56}$$

and $\beta = (a_0 + b_0)\,(a_0 - b_0)^2$. Note that $0 \le \alpha \le \alpha_0$ (the subscript 0 stands for the initial condition). The integration constant t_1 is obtained from Eq. (55) for $t = 0$. The semi-axes of the ellipse x_f and y_f are calculated from $\alpha(t)$ as

$$\begin{aligned} x_f^2(t) &= a(t) = \frac{1}{2}\left(\alpha(t) + \frac{\beta}{\alpha(t)^2}\right), \\ y_f^2(t) &= b(t) = \frac{1}{2}\left(\frac{\beta}{\alpha(t)^2} - \alpha(t)\right), \end{aligned} \tag{57}$$

and the thickness at the center, $H(t)$, is obtained from Eq. (56). Asymptotically (as $t \to \infty$), the front moves according to the radial solution given in the previous section, but with a different time shift, t_1. Thus, for $t \to \infty$ and $\alpha \ll \beta$, Eqs. (55) and (57) yield

$$x_f \approx y_f \approx 2[3\Sigma(t + t_1)]^{1/6}. \tag{58}$$

Figure 4 shows the numerical results for the evolution of the contact line, where the initial condition is specified by Eq. (53). Clearly the elliptical curves quickly become more circular as times increases, in agreement with the asymptotic solutions.

Figure 5 depicts more precisely the comparison between numerical and analytical results. This figure shows $x_f(t)$ and $y_f(t)$ resulting from three runs that use different uniform grids. The corresponding analytical solution as given by Eq. (57) is also plotted (solid lines), together with the asymptotic radial solution, Eq. (58). Clearly the numerical result closely follows the exact result. To analyze the convergence rate of the solution, we consider again the drop thickness at the origin. At $t = 10$ we have $H = 0.12769$, 0.12755, and 0.12752 for

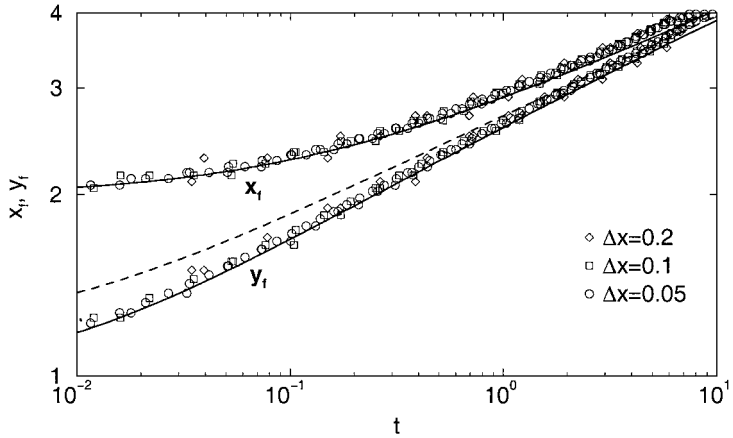

FIG. 5. Time evolution of the semi-axes $x_f(t)$ and $y_f(t)$ for the spreading of the elliptical drop in Fig. 4. The solid lines correspond to the analytical solution, Eq. (57), and the dashed line shows the asymptotic (radial) behavior, Eq. (58).

$\Delta x = 0.2, 0.1, 0.05$, respectively. The convergence is quadratic, and the theoretical value is 0.127170. The difference between the converged value and the theoretical value is due to the artificial precursor film. Once again, it decreases as $b \to 0$.

7. COALESCENCE OF SESSILE DROPS

To further illustrate the capabilities of the above-described numerical scheme, we now choose a simple but interesting problem: the coalescence of sessile drops that are simultaneously and isotropically spreading on a horizontal substrate. We concentrate on the physical case where $s = 3$.

As outlined in the Introduction, the interest in this configuration is twofold, since it involves both the contact line motion and the coalescence process. A similar problem was studied for the case of two mercury drops on a glass surface [39]. More recently, the kinetics of coalescence of two water drops on a plane solid surface was analyzed experimentally [40]. However, in those works the fluid is strongly nonwetting, while here we consider only completely wetting fluids. Furthermore, in [39] the dynamics of the drops is driven by an applied electric field, and in [40] the volume growing by condensation from the surrounding atmosphere is a major effect. Therefore, we can compare only qualitative features of the results. To our knowledge, no other experimental or theoretical results have been reported regarding this problem.

Let us consider two identical sessile drops of radius R, with centers at $(0, 0)$ and $(0, d)$ $(d > 2R)$ on a horizontal plane. After spreading, the drops begin to coalesce. The interaction between the drops breaks the radial symmetry of each drop. However, mirror symmetry with respect to the line $y = 0$ is preserved. To preserve also the mirror symmetries with respect to the perpendicular lines $x = 0$ and $x = d$, let us consider instead an infinite linear array of equidistant identical droplets, placed along the x axis and centered at $x = \ldots, -2d, -d, 0, d, 2d, \ldots$. Each drop is involved now in two simultaneous coalescence processes so that simulations can be performed only in the first quadrant; see Fig. 6. Naturally, the code can also handle the case of two isolated drops, but symmetry could not be exploited to reduce the computational domain.

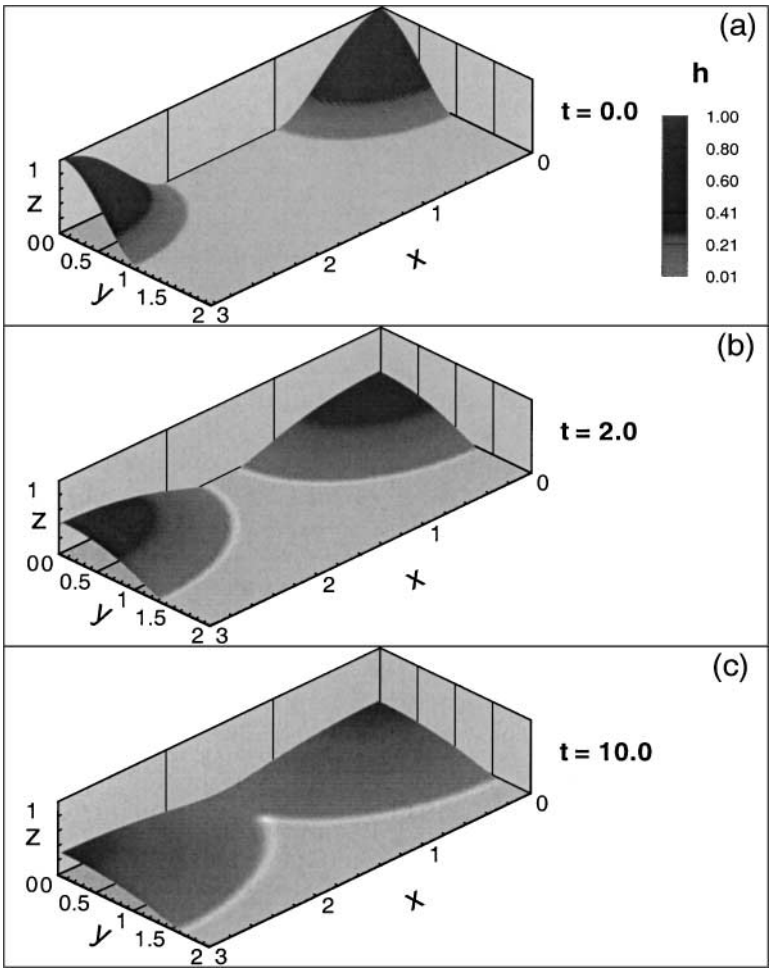

FIG. 6. Drop coalescence. (a) Initial condition, that uses mirror symmetry conditions. (b) Spreading stage. (c) Configuration during the coalescence. We use $d = 3$ and a uniform grid with $\Delta x = \Delta y = 0.025$ ($n_x = 120$, $n_y = 80$).

Both surface tension and gravity forces are relevant to this problem. We choose the scaling so that $\mathcal{C} = \mathcal{G} = 1$ in Eq. (7); i.e., $h_c = x_c = a$. Here $a = \sqrt{\gamma/\rho g}$ is the capillary length, and time t is measured in units of $t_c = 3\mu a/\gamma$;[3] since $\beta = 0$, we have $\mathcal{F} = 0$. The volume of each drop in units of a^3 is denoted by V, and we use $b = 10^{-2}$. The initial condition for the drops is given by Eq. (51), where x and y are calculated with respect to the center of each drop. The thickness H at the drop center is initially equal to unity, so that the drop volume is $V = \pi/3$.

Figure 6 shows a 3D plot of the initial condition (Fig. 6a), of the spreading (Fig. 6b), and coalescence (Fig. 6c) stages of the propagation. The spreading stage evolves similarly to the results presented in earlier works [9, 15]. In particular, a dip forms in front of the propagating front; this dip can be observed in Fig. 6 as a lighter rim around the drops and is analyzed in more detail below (see also Fig. 3 in [15]). The dynamics is significantly modified as the drops start "seeing" each other. The merging is smooth, and due to the

[3] For example, for silicon oil with $\gamma = 20$ dyn/cm, $\rho = 0.98$ g/cm^3, and $\mu = 1$ poise, we have $a = 0.14$ cm and $t_c = 0.022$ s.

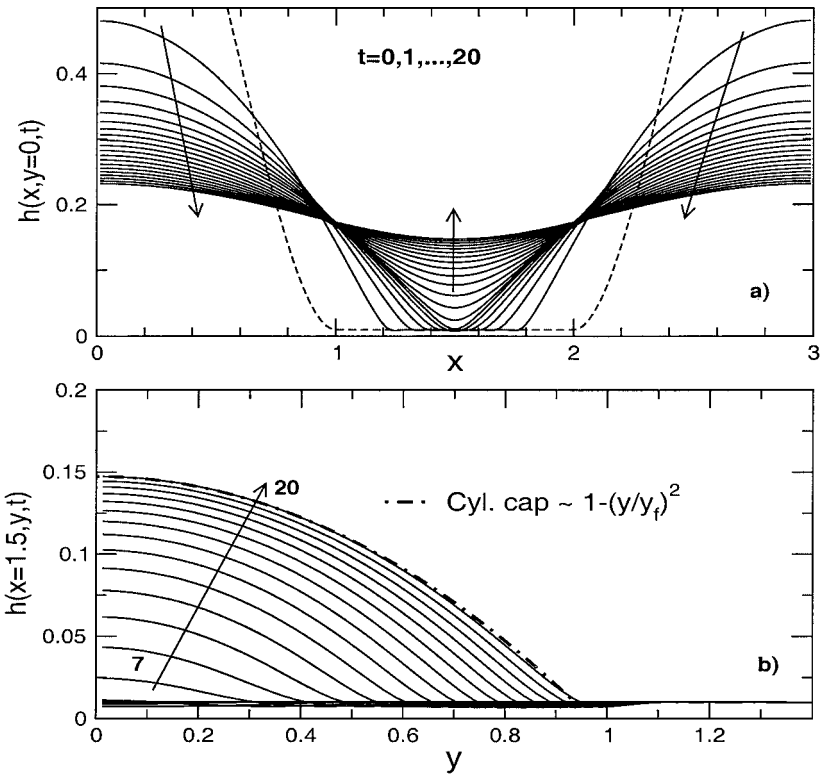

FIG. 7. (a) Thickness profile $h(x, y=0, t)$ along the symmetry line; dashed line corresponds to the initial condition, not completely visible on the scale of the figure. (b) Cross section $h(x=1.5, y, t)$ of the connecting neck at the coalescence line. The profiles are shown in $\delta t = 1$ intervals; all the parameters are as in Fig. 6. An explanation of the cylindrical cap and the definition of y_f, the front position, are given in the text. For a close-up of the coalescence region see Fig. 8.

presence of the precursor film it proceeds in a regular fashion. The coalescence process involves a transition from two contact lines to a single line enclosing both original drops.

Figure 7a shows the evolution of the fluid thickness $h(x, t)$ along the symmetry line $y = 0$. The coalescence proceeds by forming a connecting neck at $t \approx 5$ (see also Fig. 8a). Figure 7b shows how this neck widens in the y direction along $x = 1.5$. These profiles have the shape of cylindrical caps, as exemplified in Fig. 7b for $t = 20$. This behavior is typical for very small droplets [21].

Figure 8 shows a close-up of both the longitudinal and transversal profiles of the neck. To have well-resolved profiles at this short scale, we report results obtained using a nonuniform grid in the x with the smallest cell sizes located at the coalescence region (see also Section 7.1.2). As mentioned above, before the coalescence the precursor film develops a damped oscillating profile [41]. The main features of this profile are a dip of thickness $\approx 0.85b$ (visible also in Fig. 6) and a bump ahead of the dip, of height $\approx 1.01b$; see Fig. 8. The position of the dip is used below to define the location (x_f, y_f) of the contact line (front).

In Fig. 8a we see that the bumps at the fronts of the individual drops start interacting at $t \approx 3$, much earlier than the neck forms. At this time, the little bumps ahead of the dips at the fronts of each drop come into contact (see also Fig. 9a). For $3 < t < 5$, the thickness (height) of the region around $x = 1.5$ diminishes due to the arrival of the dips; see Fig. 8a.

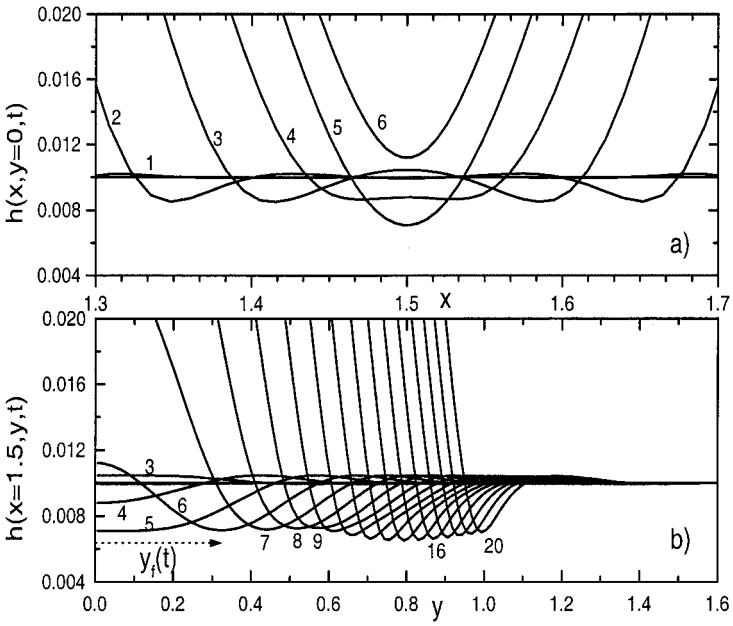

FIG. 8. Close-up of the coalescence region: (a) longitudinal and (b) cross section of the connecting neck every $\delta t = 1$. The numerical values give corresponding times; for illustration, the dashed lined marked as $y_f(t)$ shows the position of the dip defining the (half) width of the connecting neck at $t = 6$. Here we use a nonuniform grid in the x direction ($n_x = 144$, $\Delta x_{min} = 0.005$) and uniform grid in the y direction ($n_y = 160$); see Section 7.1.2.

Finally, for $t > 5$ the thickness increases and grows above b, since at this time the fluids from each drop (not only from the precursor film) are actually merging. Figure 8b shows the evolution of this profile in the y direction along the symmetry line $x = 1.5$.

Figure 9 shows more clearly the details of the early stages of drop coalescence. The merge of the little bumps ahead of the fronts leads to the formation of a minidroplet that is squeezed out of the coalescence region and starts traveling perpendicularly outward along the positive y direction (see Figs. 8b and 9b).[4] Behind this propagating minidrop, a dip region appears as a consequence of the arrival of the original dips. Thus, a new dip–bump structure is formed as a direct consequence of the coalescence process involving precursor films. Clearly, the details of this scenario of the coalescence process result from our use of precursor film to model the fluid spreading and are valid only for spreading on a prewetted surface. However, the main features of the results that follow are not model-dependent, similar to the spreading of a single drop [9].

Figure 10a shows the radii $x_f(t)$ of the circular contact lines during the spreading stage before coalescence. The dynamics of this motion has been analyzed in detail in previous works [9, 21]. Here it suffices to mention that the drop spreading proceeds by a transition from a surface tension dominated regime, where $x_f \approx t^{1/10}$, to an asymptotic gravity dominated regime with $x_f \approx t^{1/8}$ for late times. The latter regime cannot be completely reached in the presented simulations due to the presence of the second drop. For the relatively short time during which the drops spread freely, however, $x_f(t)$ can be approximated by a power law $x_f \approx Kt^{\lambda}$ with some intermediate value of λ. In Fig. 10a we see that x_f can be well fitted by $\lambda = 0.12$, except for early times when there is a strong influence of the initial condition

[4] Due to the symmetry, there would be another droplet propagating in the negative y direction.

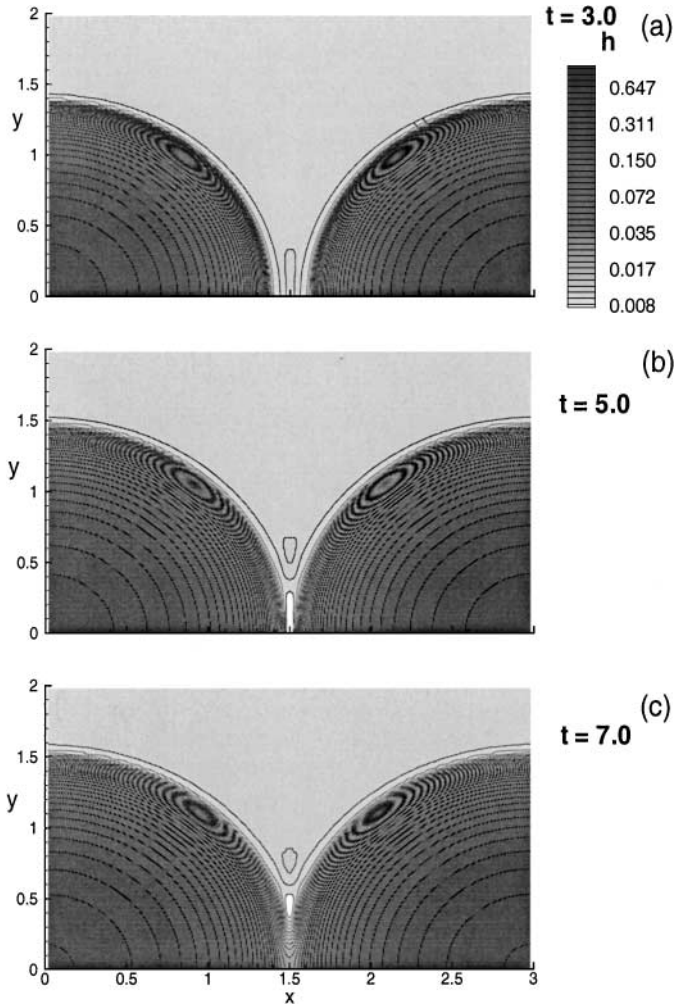

FIG. 9. Contour levels at the coalescence region showing the formation of a dip-bump structure: (a) $t = 3.0$, (b) $t = 5.0$, and (c) $t = 7.0$. Note the formation of a bump in the coalescence region (a) followed by a dip (b,c) [42].

on the spreading rate. The prefactor K is obtained by requiring that $x_f(t_{coal}) = 1.5$, where the coalescence time $t_{coal} \approx 4.9$, as motivated below.

Figure 10b shows the half width of the neck, y_f, defined as the dip position in the dip–bump structure described above (see Figs. 8b and 9). Note that $t = 4.9$ is the time at which the connecting neck is first captured. The behavior of $y_f(t)$ for early times after coalescence can be understood by comparing it with the spreading of a *single* drop. In that case, the y position of the contact line at $x = 1.5$ is given by $(y_f)_{single} = \sqrt{x_f^2 - 1.5^2}$. Using the power law for x_f as given above, we obtain the dashed line in Fig. 10b. The agreement with $y_f(t)$ is very good even up to times as long as $t \approx 9$. This shows, perhaps surprisingly, that even for relatively late times the coalescence process is strongly influenced by the dynamics of the original drops.

Figure 10b also shows the thickness of the neck, $h_0(t) = h(1.5, 0, t)$. The coalescence process described above is manifested here as a slight increase of h_0 at $t \approx 3$ (bumps

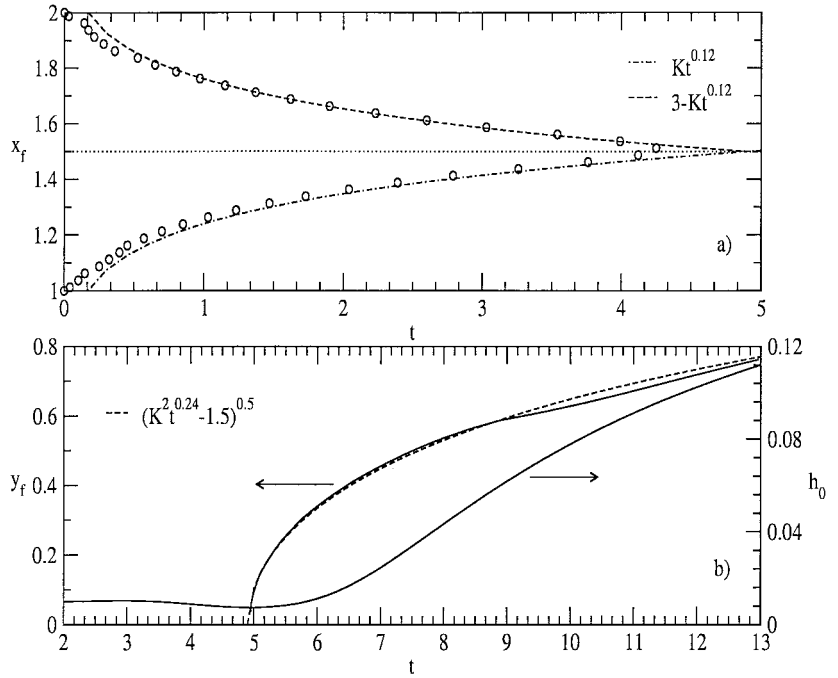

FIG. 10. (a) Front position $x_f(t)$ for the radial spreading of the drops; the power-law fits are explained in the text. (b) Half width, $y_f(t)$, and thickness, $h_0(t)$, of the connecting neck for the case shown in Fig. 6. The broken line shows the propagation of the contact line of a single drop in the y direction at $x = 1.5$ (see text).

interaction), a local minimum at $t \approx 5$ (dips arrival), and a monotonous increase for later times (drops coalescence itself). This curve is qualitatively similar to those reported in Fig. 9 of [39] for the coalescence of two mercury drops. To our knowledge, no other documented experimental nor numerical results exist for the evolution of this quantity.

Figure 11 shows how $h_0(t)$ depends on the thickness of the precursor film, b. As expected, the curves are qualitatively similar; the main difference is that they are shifted in time, besides being displaced vertically due to different b values. This shift is due to a decreased viscous dissipation rate for larger b's, resulting in larger front velocities and earlier coalescence.

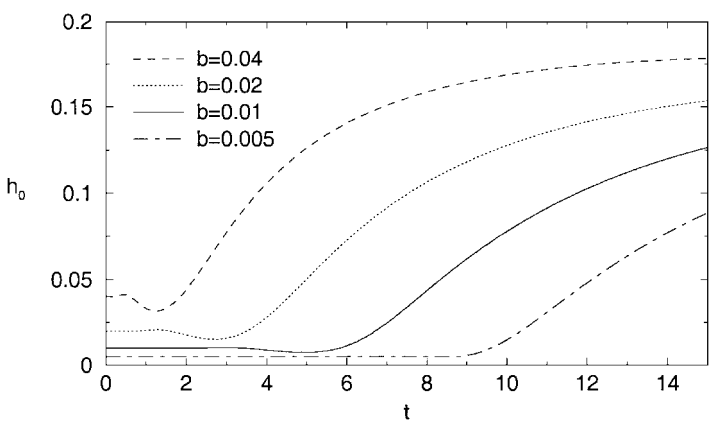

FIG. 11. Thickness h_0 of the connecting neck as a function of time for different values of the precursor film b.

7.1. Convergence Properties

The main goal of the presentation that follows is to explore the convergence properties of various uniform and nonuniform discretizations. Since our numerical method allows us to implement any of these two possibilities in either direction, we will be able to discuss the resolution needed for converged results, as well as the appropriateness of computing on nonuniform grids. We take the time evolution of the fluid thickness at the coalescence point, $h_0(t)$, as a testing parameter, since it is a very sensitive measure of the quality of the solution.

7.1.1. *Uniform Grid*

Figure 12 shows $h_0(t)$ computed by using uniform grids; in Fig. 12a Δx is changed, and in Fig. 12b we modify Δy (see also Table I). In these calculations the time step is varied following the requirements of Section 5.1 with $\mathrm{Tol} = 10^{-2}$. The solid line in both parts corresponds to the most resolved case for each set. It is interesting to observe that convergence in the x direction proceeds from smaller values of h_0, while the y convergence is achieved starting from larger values.

Table I shows more precisely how the results converge as the number of grid points is increased, separately in the x and y directions. To estimate the rate of convergence, we calculate the ratio of the differences of h_0^* values computed using a different number of grid points; see Section 7.2 for more details. These ratios should be approximately equal to 4 for a second-order method. The results shown in Table I give the values 4.04 and 4.86 for the x and y directions, respectively. We note also that for not too large numbers of grid points, CPU time grows according to $t_{cpu} \sim N \log N$, where N is the total number of points. There are several factors that influence t_{cpu}, including accuracy requirements, the number of Newton iterations needed for convergence, as well as the number of iterations of our biconjugate gradient method. For very large N, these factors lead to faster growth of t_{cpu}.

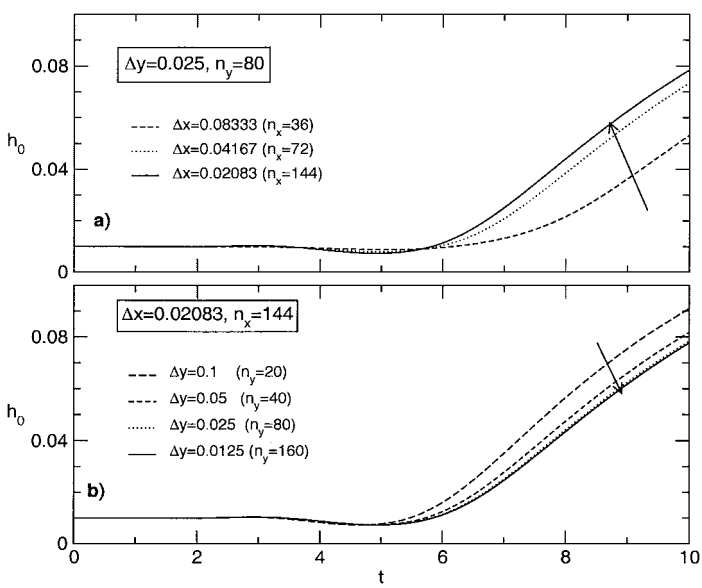

FIG. 12. Thickness of the connecting neck $h_0(t)$ as obtained using different uniform grids: (a) Δx is varied ($\Delta y = \text{const.}$); (b) Δy is varied ($\Delta x = \text{const.}$). The arrows show the direction of decreasing Δx and Δy, respectively.

TABLE I

Thickness of the Neck at $t = 10$ ($h_0^* = 10^2 h_0(t = 10)$), and the Corresponding CPU Time in Seconds for Different Uniform Grids (Calculations Performed on an SGI Origin 2000 Server)

n_x	Δx	n_y	Δy	h_0^*	CPU time
36	0.08333	80	0.025	5.32	2937
72	0.04167	80	0.025	7.34	6982
144	0.02083	80	0.025	7.84	24687
144	0.02083	20	0.1	9.10	4309
144	0.02083	40	0.05	8.18	9384
144	0.02083	80	0.025	7.84	24687
144	0.02083	160	0.0125	7.77	112465

Note. Quadratic convergence of h_0^* is obtained in both sets.

In a typical run, performed using a variable time step, the number of Newton iterations is about 2–3, with the number of biconjugate gradient iterations decreasing significantly throughout a simulation, most probably due to weaker gradients of the numerical solution for later times. This number is typically of the form N/F, with F varying between 10 and 100.

To analyze the effects related to the use of a variable time step, we also perform calculations using different *fixed* time steps (see Table II). Clearly, the use of a variable time step has a major influence on the performance of our method: it reduces significantly the CPU time, while modifying at most the fourth digit of the h_0^* values. These results also show that the accuracy requirements specified in Section 5.1 are sufficient for this problem.

7.1.2. *Nonuniform Grid*

Next we perform convergence checks using nonuniform grids, with the goal of increasing accuracy without unnecessarily increasing the computational effort. The region that clearly needs more accurate discretization is around the merging zone, $x = 1.5$ and $y = 0$. Therefore, we perform two kinds of checks: (1) Analysis of x convergence, where we choose Δx_{min} at the coalescence line $x = 1.5$ (with the maximum values located at the boundaries $x = 0$ and $x = 3$), while holding Δy uniform; (2) analysis of y convergence, where Δy_{min} is set at $y = 0$ (with Δy_{max} at $y = 2$), and Δx is uniform.

TABLE II

Thickness $h_0^* = 10^2 h_0(t = 10)$ and CPU Time in Seconds Showing the Advantages of Using Variable Δt and Its Small Effect on the Results; $n_x = 144$

	n_y		
Δt	20	40	80
Variable	9.09890/4309	8.18205/9385	7.84436/24687
10^{-2}	9.09868/7550	8.18161/17808	7.84408/49576
10^{-3}	9.09872/22888	8.18165/50426	7.84404/138083
10^{-4}	9.09875/86571	8.18169/188591	7.84404/504200

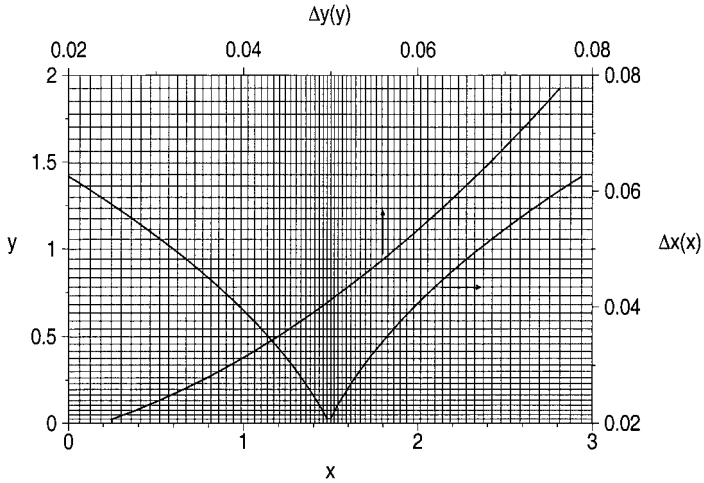

FIG. 13. Sketch of a nonuniform grid, and the (quadratic) curves for the cell size as a function of x and y (coordinates of the (i, j) corner of the cell; see Fig. 1). Here, $n_x = 74$ and $n_y = 40$ with $\Delta x_{min} = 0.02083$ at $x = 1.5$ and $\Delta y_{min} = 0.025$ at $y = 0$.

In all cases, our mesh generator produces nonuniform grids with quadratic dependence of the cell size on the spatial variable. Figure 13 shows an example of a mesh nonuniform in both directions, together with the corresponding quadratic curves $\Delta x(x)$ and $\Delta y(y)$. If Δx_{min} is reduced, and the number of cells is kept fixed, we obtain steeper curves $\Delta x(x)$, and both the cell concentration around Δx_{min} and the value of Δx_{max} increase. On the other hand, if n_x is increased while Δx_{min} is fixed, the contrary effect is obtained. In the limit of very large n_x, the curve tends to $\Delta x(x) = \Delta x_{min} = \text{const.}$, so that the mesh becomes uniform; the same holds in the y direction.

Figure 14 shows the results for $h_0(t)$, where the number of grid points (n_x and n_y, respectively) is varied, while the corresponding minimum values (Δx_{min} and Δy_{min}) are

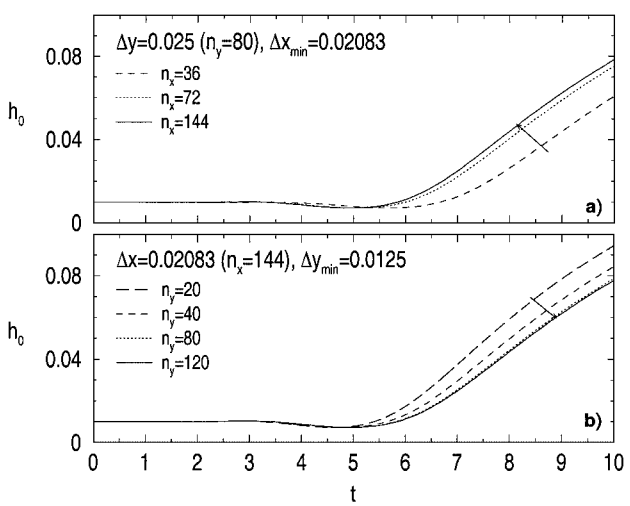

FIG. 14. Thickness of the connecting neck $h_0(t)$ as obtained for different *nonuniform* grids: (a) nonuniform in x, uniform in y; (b) uniform in y, nonuniform in x. The arrows point in the direction of increasing n_x and n_y, respectively.

TABLE III

Thickness $h_0^* = 10^2 h_0(t = 10)$ and CPU Time in Seconds, as n_x for a Nonuniform x Grid Is Varied; $\Delta y = 0.0125$ ($n_y = 160$)

n_x	Δx_{min}	h_0^*	CPU time
36	0.02083	6.02	21866
72	0.02083	7.45	46362
144	0.02083	7.77	112465

kept fixed. The most resolved case is shown by the solid line in Fig. 14, and by the last row in Tables III and IV. To verify quadratic convergence, we double the number of grid points and calculate the ratio of the differences of h_0^*, similar to the uniform grid case. These ratios are 4.61 and 5.70 for the sets in Tables III and IV, respectively.

We have also performed runs using fixed n_x (n_y) and decreasing Δx_{min} (Δy_{min}) with uniform grid in the y (x) direction. For brevity we do not show plots for this case because the differences among the results are very small. In these cases, we also obtain a quadratic convergence rate for h_0^*.

7.2. Numerical Performances

In this section we investigate the relative performances of the computations performed on uniform and nonuniform grids. In general, there is no clear rule on whether a uniform or nonuniform grid is more efficient. This certainly depends on the problem at hand and has to be investigated separately in each case.

Usually, nonuniform grids can be of advantage if the solution varies slowly almost everywhere, while the interesting aspects of the problem are limited to a small portion of the domain. This is not clear a priori in our problem, since it involves two different phenomena: contact line motion and coalescence itself. Both of these processes are sensitive to the mesh size; for instance, if for a given number of points one chooses a finer grid at the coalescence point, then the results can lose accuracy because of the coarse grid used to compute the contact line motion elsewhere.

TABLE IV

Thickness $h_0^* = 10^2 h_0(t = 10)$ and CPU Time in Seconds, as n_y for a Nonuniform y Grid Is Varied with $\Delta x = 0.02083$ ($n_x = 144$)

n_y	Δy_{min}	h_0^*	CPU time
20	0.0125	9.46	16919
40	0.0125	8.44	13078
80	0.0125	7.87	33120
160	0.0125	7.77	112465

Note. The case $n_y = 160$ is coincident with the uniform case in the last row of Table I, because for this large n_y, $\Delta y_{max} = \Delta y_{min}$.

To decide in favor of one kind of grid, one can compare the computational effort needed to perform calculations that lead to the same *quality* (accuracy) of the results. Conversely, one can also make a comparison of the accuracy under the same *number of cells*; this is what we do here. To compare accuracies we take as the most accurate solution that given by the well-resolved case with uniform grid; namely, $n_x = 144$ and $n_y = 160$. This grid will be denoted by $(144u, 160u)$, where u means that the grid is uniform in the corresponding direction; n will be used to denote a nonuniform grid. For uniform grids, and at $t = 10$, we obtain

$$|h_0^*(144u, 160u) - h_0^*(72u, 160u)| = 0.50$$
$$|h_0^*(144u, 160u) - h_0^*(36u, 160u)| = 2.5.$$

Equivalent differences for nonuniform grids and the same n_x are

$$|h_0^*(144u, 160u) - h_0^*(72n, 160u)| = 0.32$$
$$|h_0^*(144u, 160u) - h_0^*(36n, 160u)| = 1.7.$$

We see that, in general, a *nonuniform* grid in the x direction yields results which are more accurate than the uniform grid that uses the same number of cells. Furthermore, this greater accuracy is obtained using less CPU time, as seen in Tables I and III. Therefore, from these results we conclude that it is more efficient to use a *nonuniform* x grid for this problem.

Next, we perform a similar comparison for the y direction. In this case, we obtain

$$|h_0^*(144u, 160u) - h_0^*(144u, 80u)| = 0.07$$
$$|h_0^*(144u, 160u) - h_0^*(144u, 40u)| = 0.41.$$

The equivalent differences for a nonuniform grid in the y direction are

$$|h_0^*(144u, 160u) - h_0^*(144u, 80n)| = 0.10$$
$$|h_0^*(144u, 160u) - h_0^*(144u, 40n)| = 0.67.$$

In this case, the differences are in favor of the *uniform* grid. Also, CPU times are much smaller for uniform than for nonuniform y grids (see Tables I and IV).

In summary, based on the numerical effort required for a given accuracy, we conclude that the use of a nonuniform x grid and a uniform y grid is advisable for the present problem. This result can be understood by observing the geometry of the problem. A nonuniform grid in the x direction resolves well the most critical area ($x = 1.5$) along which the coalescence of the drops occurs. A nonuniform grid in y, on the other hand, resolves well only the zone about $y = 0$, where just the *initial* part of the coalescence takes place.

8. SUMMARY AND CONCLUSIONS

We have developed a computational method for quasi 3D unsteady coating flows. In this work, we applied this method to the spreading and coalescence of an incompressible

fluid on a horizontal substrate; the simulations of flows on inclined planes were presented elsewhere (see [14–16]).

The first part of this paper explained in some detail the computational issues involved in modeling thin film flows in higher dimensions. In particular, we presented an efficient approach to perform computations on nonuniform Cartesian grids. As a result, we were able to address the evolution of features characterized by very short length scales, as exemplified in Section 7. The numerical method was validated by using the problems for which analytical solutions exist. These problems were obtained by setting the exponent, s, of the coefficient of fourth-order capillary terms to $s = 1$. Careful analysis has shown quadratic convergence to the exact solution for both radial and elliptic drops.

The second part of this work combined the two main issues that are relevant in understanding of thin film flows: (1) contact line paradox and (2) topology changes, such as coalescence or rupture. We approached both of these issues by using a precursor film model and illustrated how it allows us to proceed smoothly through the process of coalescence of two sessile drops spreading on a horizontal substrate. In particular, we focused on the description of the connecting neck that develops in the contact region. We observed that the merging process comprises two stages, one being the early interaction of the dip–bump structure of the front region of each drop and the other the coalescence itself, involving the fluid from the bulks. Interestingly enough, as a result of this interaction a new dip–bump-isolated structure is formed at the coalescence line. This structure spans in both directions and travels outward ahead of the connecting neck. This is a novel feature of the problem, and it has been observed in our simulations solely due to a very fine resolution of the critical region of the flow, resolved using nonuniform meshes. While this dip–bump structure is a direct consequence of the presence of the precursor film, the results for other properties of the flow are more general. In particular, the evolution of the height and of the width of the connecting neck as well as the transversal and longitudinal thickness profiles depend (weakly) only on the length scales introduced at the contact lines, but not on the model itself. Therefore, it is expected that the results regarding the dynamics of these quantities can be confirmed by experiment. The work in this direction is currently in progress.

Going back to the computational issues, our analysis shows that, while nonuniform grids are very useful to analyze the dynamics of localized structures in the flow, one has to be careful of their use. In particular, for the problem of drop merging, the use of a nonuniform grid in the direction connecting the drop centers, and of a uniform grid in the normal direction is most advisable from the viewpoint of numerical efficiency.

Additional usefulness of the presented numerical scheme is due to fact that it allows for easy inclusion of other physical effects. These can be accounted for by forces as different as thermocapillary (Marangoni effect), electrical, inertial (e.g., centrifugal), or intermolecular (van der Waals interaction). The computational studies of problems in these areas are currently being performed.

APPENDIX A: COEFFICIENTS FOR NONUNIFORM GRIDS

We present here the general expressions for the coefficients $L_l^{(m)}$, $R_l^{(m)}$, $B_l^{(m)}$, and $T_l^{(m)}$ ($1 \le m \le 7$, $-6 \le l \le 6$) for a nonuniform, Cartesian grid, which result from a centered finite difference scheme applied to each term of Eq. (7).

Surface Tension Term

The coefficients $L_l^{(1)}$ and $R_l^{(1)}$ defined in Eq. (12) are

$$\begin{aligned}
L_{-2}^{(1)} &= \frac{q_x}{\Delta x_{i-1}\Delta x_{i-1}^c \Delta x_i} \\
L_{-1}^{(1)} &= \frac{-q_x}{\Delta x_i}\left(\frac{1}{\Delta x_i^c \Delta x_i} + \frac{1}{\Delta x_{i-1}^c \Delta x_i} + \frac{1}{\Delta x_{i-1}^c \Delta x_{i-1}}\right) \\
R_{-1}^{(1)} &= \frac{-q_x}{\Delta x_{i+1}\Delta x_i^c \Delta x_i} \\
L_0^{(1)} &= \frac{q_x}{\Delta x_i}\left(\frac{1}{\Delta x_i^c \Delta x_{i+1}} + \frac{1}{\Delta x_i^c \Delta x_i} + \frac{1}{\Delta x_{i-1}^c \Delta x_i}\right) \\
R_0^{(1)} &= \frac{q_x}{\Delta x_{i+1}}\left(\frac{1}{\Delta x_{i+1}^c \Delta x_{i+1}} + \frac{1}{\Delta x_i^c \Delta x_{i+1}} + \frac{1}{\Delta x_i^c \Delta x_i}\right) \\
L_1^{(1)} &= \frac{-q_x}{\Delta x_{i+1}\Delta x_i^c \Delta x_i} \\
R_1^{(1)} &= \frac{-q_x}{\Delta x_{i+1}}\left(\frac{1}{\Delta x_{i+1}^c \Delta x_{i+2}} + \frac{1}{\Delta x_{i+1}^c \Delta x_{i+1}} + \frac{1}{\Delta x_i^c \Delta x_{i+1}}\right), \\
R_2^{(1)} &= \frac{q_x}{\Delta x_{i+1}\Delta x_{i+1}^c \Delta x_{i+2}},
\end{aligned} \tag{59}$$

where

$$\Delta x_i^c = \frac{\Delta x_i + \Delta x_{i+1}}{2}. \tag{60}$$

and

$$q_x = \frac{1}{\Delta x_i^c}. \tag{61}$$

For the simpler uniform grid case they become

$$\begin{aligned}
&L_{-2}^{(1)} = 1/\Delta x_i^4, \quad L_{-1}^{(1)} = -3/\Delta x_i^4, \quad R_{-1}^{(1)} = -1/\Delta x_i^4, \\
&L_0^{(1)} = 3/\Delta x_i^4, \quad R_0^{(1)} = 3/\Delta x_i^4, \\
&L_1^{(1)} = -1/\Delta x_i^4, \quad R_1^{(1)} = -3/\Delta x_i^4, \quad R_2^{(1)} = 1/\Delta x_i^4.
\end{aligned} \tag{62}$$

As mentioned in the text, the coefficients $B_l^{(2)}$ and $T_l^{(2)}$ are obtained from Eq. (59) by changing Δx_i to Δy_j.

The coefficients $L_l^{(3)}$ and $R_l^{(3)}$ defined in Eq. (18) are

$$\begin{aligned}
L_{-5}^{(3)} &= \frac{q_{xy}}{\Delta x_i \Delta y_j}, \quad L_{-4}^{(3)} = \frac{-q_{xy}}{\Delta x_i \Delta y_j}, \\
R_{-4}^{(3)} &= \frac{-q_{xy}}{\Delta x_{i+1}\Delta y_j}, \quad R_{-3}^{(3)} = \frac{q_{xy}}{\Delta x_{i+1}\Delta y_j}, \\
L_{-1}^{(3)} &= \frac{-q_{xy}}{\Delta x_i}\left(\frac{1}{\Delta y_j} + \frac{1}{\Delta y_{j+1}}\right),
\end{aligned}$$

$$L_0^{(3)} = \frac{q_{xy}}{\Delta x_i}\left(\frac{1}{\Delta y_j} + \frac{1}{\Delta y_{j+1}}\right),$$
$$R_0^{(3)} = \frac{q_{xy}}{\Delta x_{i+1}}\left(\frac{1}{\Delta y_j} + \frac{1}{\Delta y_{j+1}}\right),$$
$$R_1^{(3)} = \frac{-q_{xy}}{\Delta x_{i+1}}\left(\frac{1}{\Delta y_j} + \frac{1}{\Delta y_{j+1}}\right),$$
$$L_3^{(3)} = \frac{q_{xy}}{\Delta x_i \Delta y_{j+1}}, \quad R_5^{(3)} = \frac{q_{xy}}{\Delta x_{i+1}\Delta y_{j+1}},$$
$$L_4^{(3)} = \frac{-q_{xy}}{\Delta x_i \Delta y_j}, \quad R_4^{(3)} = \frac{-q_{xy}}{\Delta x_{i+1}\Delta y_{j+1}},$$

where

$$q_{xy} = \frac{1}{\Delta x_i^c \Delta y_j^c}, \quad \Delta y_j^c = \frac{\Delta y_j + \Delta y_{j+1}}{2}.$$

The coefficients $B_l^{(4)}$ and $T_l^{(4)}$ are obtained by changing $\Delta x_i \leftrightarrow \Delta y_j$.

Normal Gravity Terms

The coefficients $L_l^{(5)}$ and $R_l^{(5)}$ defined in Eq. (29) are

$$L_{-1}^{(5)} = \frac{q_x}{\Delta x_i}, \quad R_1^{(5)} = \frac{q_x}{\Delta x_{i+1}}$$
$$L_0^{(5)} = -\frac{q_x}{\Delta x_i}, \quad R_0^{(5)} = -\frac{q_x}{\Delta x_{i+1}}.$$

Analogously, the coefficients $B_l^{(6)}$ and $T_l^{(6)}$ defined in Eq. (31) are

$$B_{-2}^{(6)} = \frac{q_y}{\Delta y_j}, \quad T_2^{(6)} = \frac{q_y}{\Delta y_{j+1}},$$
$$B_0^{(6)} = \frac{-q_y}{\Delta y_j}, \quad T_0^{(6)} = \frac{-q_y}{\Delta y_{j+1}},$$

where

$$q_y = \frac{1}{\Delta y_j^c}.$$

Parallel Gravity Term

The coefficients $L_l^{(7)}$ and $R_l^{(7)}$ defined in Eq. (29) are

$$L_{-1}^{(7)} = \frac{-q_x}{2}, \quad R_1^{(7)} = \frac{q_x}{2},$$
$$L_0^{(7)} = \frac{-q_x}{2}, \quad R_0^{(7)} = \frac{q_x}{2},$$

APPENDIX B: JACOBIAN

The elements of the Jacobian needed for the Newton–Kantorovich's method (see Eq. (44)) are given by

$$\begin{aligned}
F_{k,-6} &= \frac{\partial f_k}{\partial h_{k-2n_x}} = a_{k,-6}, \quad F_{k,-5} = \frac{\partial f_k}{\partial h_{k-n_x-1}} = a_{k,-5},\\
F_{k,-3} &= \frac{\partial f_k}{\partial h_{k-n_x+1}} = a_{k,-3}, \quad F_{k,-2} = \frac{\partial f_k}{\partial h_{k-2}} = a_{k,-2},\\
F_{k,2} &= \frac{\partial f_k}{\partial h_{k+2}} = a_{k,2}, \quad F_{k,3} = \frac{\partial f_k}{\partial h_{k+n_x-1}} = a_{k,3},\\
F_{k,5} &= \frac{\partial f_k}{\partial h_{k+n_x+1}} = a_{k,5}, \quad F_{k,6} = \frac{\partial f_k}{\partial h_{k+2n_x}} = a_{k,6},
\end{aligned} \tag{63}$$

and

$$\begin{aligned}
F_{k,-4} &= \frac{\partial f_k}{\partial h_{k-n_x}} = a_{k,-4} + \frac{\partial D^{(y)}_{k-n_x}}{\partial h_{k-n_x}} A_{-4} + \frac{\partial G^{(y)}_{k-n_x}}{\partial h_{k-n_x}} \hat{A}_{-4}\\
F_{k,-1} &= \frac{\partial f_k}{\partial h_{k-1}} = a_{k,-1} + \frac{\partial D^{(x)}_{k-1}}{\partial h_{k-1}} A_{-1} + \frac{\partial G^{(x)}_{k-1}}{\partial h_{k-1}} \hat{A}_{-1} + \frac{\partial H_{k-1}}{\partial h_{k-1}} \tilde{A}_{-1}\\
F_{k,0} &= \frac{\partial f_k}{\partial h_k} = a_{k,0} + \frac{\partial D^{(y)}_{k-n_x}}{\partial h_k} A_{-4} + \frac{\partial D^{(x)}_{k-1}}{\partial h_k} A_{-1} + \frac{\partial D^{(x)}_{k}}{\partial h_k} A_{1}\\
&\quad + \frac{\partial D^{(y)}_{k}}{\partial h_k} A_{4} + \frac{\partial G^{(x)}_{k-1}}{\partial h_k} \hat{A}_{-1} + \frac{\partial G^{(y)}_{k-n_x}}{\partial h_k} \hat{A}_{-4}\\
F_{k,1} &= \frac{\partial f_k}{\partial h_{k+1}} = a_{k,1} + \frac{\partial D^{(x)}_{k}}{\partial h_{k+1}} A_{1} + \frac{\partial G^{(x)}_{k}}{\partial h_{k+1}} \hat{A}_{1} + \frac{\partial H_{k}}{\partial h_{k+1}} \tilde{A}_{1},\\
F_{k,4} &= \frac{\partial f_k}{\partial h_{k+n_x}} = a_{k,4} + \frac{\partial D^{(y)}_{k}}{\partial h_{k+n_x}} A_{4} + \frac{\partial G^{(x)}_{k}}{\partial h_{k+1}} \hat{A}_{4}.
\end{aligned} \tag{64}$$

Here, the A's are related to the surface tension terms, while the $\hat{A}$'s and $\tilde{A}$'s correspond to the normal and parallel gravity terms, respectively. They are given by

$$\begin{aligned}
A_{-4} &= B_{k,-6} h_{k-2n_x} + B_{k,-5} h_{k-n_x-1} + B_{k,-4} h_{k-n_x} + B_{k,-3} h_{k-n_x+1}\\
&\quad + B_{k,0} h_k + B_{k,1} h_{k+1} + B_{k,4} h_{k+n_x}\\
A_{-1} &= L_{k,-5} h_{k-n_x-1} + L_{k,-4} h_{k-n_x} + L_{k,-2} h_{k-2} + L_{k,-1} h_{k-1}\\
&\quad + L_{k,1} h_{k+1} + L_{k,3} h_{k+n_x-1} + L_{k,4} h_{k+n_x}\\
A_{1} &= R_{k,-4} h_{k-n_x} + R_{k,-3} h_{k-n_x+1} + R_{k,-1} h_{k-1} + R_{k,0} h_k + R_{k,1} h_{k+1}\\
&\quad + R_{k,2} h_{k+2} + R_{k,4} h_{k+n_x} + R_{k,5} h_{k+n_x+1}\\
A_{4} &= T_{k,-4} h_{k-n_x} + T_{k,-1} h_{k-1} + T_{k,0} h_k + T_{k,1} h_{k+1} + T_{k,3} h_{k+n_x-1}\\
&\quad + T_{k,4} h_{k+n_x} + T_{k,5} h_{k+n_x+1} + T_{k,6} h_{k+2n_x},
\end{aligned} \tag{65}$$

and

$$\begin{aligned}
\hat{A}_{-4} &= \hat{B}_{k,0}h_k + \hat{B}_{k,-2}h_{k+n_x}, \quad \hat{A}_{-1} = \hat{L}_{k,-1}h_{k-1} + \hat{L}_{k,0}h_k, \\
\hat{A}_1 &= \hat{R}_{k,0}h_k + \hat{R}_{k,1}h_{k+1}, \quad \hat{A}_4 = \hat{T}_{k,0}h_k + \hat{T}_{k,2}h_{k+n_x}, \\
\tilde{A}_1 &= \tilde{R}_{k,0}h_k + \tilde{R}_{k,1}h_{k+1}, \quad \tilde{A}_{-1} = \tilde{L}_{k,-1}h_{k-1} + \tilde{L}_{k,0}h_k.
\end{aligned} \tag{66}$$

The derivatives of the nonlinear coefficients due to the surface tension term required to evaluate Eq. (64) are given by

$$\begin{aligned}
\frac{\partial D_k^{(x)}}{\partial h_k} &= \frac{-D_k^{(x)}}{h_{k+1} - h_k}\left(1 - \frac{D_k^{(x)}}{h_k^3}\right), \\
\frac{\partial D_k^{(x)}}{\partial h_{k+1}} &= \frac{D_k^{(x)}}{h_{k+1} - h_k}\left(1 - \frac{D_k^{(x)}}{h_{k+1}^3}\right), \\
\frac{\partial D_k^{(y)}}{\partial h_k} &= \frac{-D_k^{(y)}}{h_{k+n_x} - h_k}\left(1 - \frac{D_k^{(y)}}{h_k^3}\right), \\
\frac{\partial D_k^{(y)}}{\partial h_{k+n_x}} &= \frac{D_k^{(y)}}{h_{k+n_x} - h_k}\left(1 - \frac{D_k^{(y)}}{h_{k+n_x}^3}\right)
\end{aligned} \tag{67}$$

while for both gravity terms the calculation of the corresponding derivatives is straightforward from Eqs. (27) and (35).

ACKNOWLEDGMENTS

The authors thank Andrew Bernoff and Thomas Witelski for useful comments. J. D. acknowledges the Fulbright Foundation, NJIT, and Consejo Nacional de Investigaciones Científicas y Técnicas (CONICET-Argentina) for supporting his visit to NJIT. The authors acknowledge the support from NSF Grant INT-0122911, and L. K. the support from NJIT Grant 421210.

REFERENCES

1. N. Fraysse and G. M. Homsy, An experimental study of rivulet instabilities in centrifugal spin coating of viscous Newtonian and non-Newtonian fluids, *Phys. Fluids* **6**, 1491 (1994).
2. F. Melo, J. F. Joanny, and S. Fauve, Fingering instability of spinning drops, *Phys. Rev. Lett.* **63**, 1958 (1989).
3. A. M. Cazabat, F. Heslot, S. M. Troian, and P. Carles, Finger instability of this spreading films driven by temperature gradients, *Nature* **346**, 824 (1990).
4. M. J. Tan, S. G. Bankoff, and S. H. Davis, Steady thermocapillary flows of thin liquid layers. I. Theory, *Phys. Fluids A* **2**, 313 (1990).
5. X. Fanton, A. M. Cazabat, and D. Quéré, Thickness and shape of films driven by a Marangoni flow, *Langmuir* **12**, 5875 (1996).
6. A. Oron, S. H. Davis, and S. G. Bankoff, Long-scale evolution of thin liquid films, *Rev. Mod. Phys.* **69**, 931 (1997).
7. E. B. Dussan V., On the spreading of liquids on solid surfaces: Static and dynamic contact lines, *Annu. Rev. Fluid Mech.* **11**, 317 (1979).
8. P. G. de Gennes, Wetting: Statics and dynamics, *Rev. Mod. Phys.* **57**, 827 (1985).

9. J. Diez, L. Kondic, and A. L. Bertozzi, Global models for moving contact lines, *Phys. Rev. E* **63**, 011208 (2001).
10. M. H. Eres, L. W. Schwartz, and R. V. Roy, Fingering phenomena for driven coating films, *Phys. Fluids* **12**, 1278 (2000).
11. T. P. Witelski and M. Bowen, ADI schemes for higher-order nonlinear diffusion equations, *J. Applied Num. Math.*, to appear.
12. D. T. Moyle, M. S. Chen, and G. M. Homsy, Nonlinear rivulet dynamics during unstable dynamic wetting flows, *Int. J. Mult. Flow* **25**, 1243 (1999).
13. Y. Ye and H. Chang, A spectral theory for fingering on a prewetted plane, *Phys. Fluids* **11**, 2494 (1999).
14. J. Diez and L. Kondic, Contact line instabilites of thin liquid films, *Phys. Rev. Lett.* **86**, 632 (2001).
15. L. Kondic and J. Diez, Contact line instabilities of thin film flows: Constant flux configuration, *Phys. Fluids* **13**, 3168 (2001).
16. L. Kondic and J. Diez, Flow of thin films on patterned surfaces: Controlling the instability, *Phys. Rev. E* **65**, 045301 (2002).
17. M. Renardy, Y. Renardy, and J. Li, Numerical simulation of moving contact line problems using a volume-of-fluid method, *J. Comput. Phys.* **171**, 243 (2001).
18. G. Grün and M. Rumpf, Simulation of singularities and instabilities arising in thin film flow, *Eur. J. Appl. Math.* **12**, 293 (2001).
19. H. P. Greenspan, On the motion of a small viscous droplet that wets a surface, *J. Fluid Mech.* **84**, 125 (1978).
20. A. M. Cazabat and C. Stuart, Dynamics of wetting: Effects of surface roughness, *J. Phys. Chem.* **90**, 5845 (1986).
21. R. Gratton, J. Diez, L. P. Thomas, B. Marino, and S. Betelú, Quasi-self-similarity for wetting drops, *Phys. Rev. E* **53**, 3563 (1996).
22. J. Eggers, J. R. Lister, and H. A. Stone, Coalescence of liquid drops, *J. Fluid Mech.* **401**, 293 (1999).
23. R. W. Hopper, Coalescence of two viscous cylinders by capillarity: Part I. Theory, *J. Amer. Ceram. Soc.* **76**, 2947 (1993).
24. R. W. Hopper, Coalescence of two viscous cylinders by capillarity: Part II. Shape evolution, *J. Amer. Ceram. Soc.* **76**, 2953 (1993).
25. Y. D. Shikhmurzaev, Coalescence and capillary breakup of liquid volume, *Phys. Fluids* **12**, 2386 (2000).
26. V. Cristini, J. Blawsdziewics, and M. Loewenberg, An adaptive mesh algorithm for evolving surfaces: Simulations of drop breakup and coalescence, *J. Comput. Phys.* **168**, 445 (2001).
27. S. M. Troian, E. Herbolzheimer, S. A. Safran, and J. F. Joanny, Fingering instabilities of driven spreading films, *Europhys. Lett.* **10**, 25 (1989).
28. A. L. Bertozzi and M. P. Brenner, Linear stability and transient growth in driven contact lines, *Phys. Fluids* **9**, 530 (1997).
29. M. A. Spaid and G. M. Homsy, Stability of Newtonian and viscoelastic dynamic contact lines, *Phys. Fluids* **8**, 460 (1996).
30. Dussan V., E. B., The moving contact line: The slip boundary condition, *J. Fluid Mech.* **77**, 665 (1976).
31. L. M. Hocking and A. D. Rivers, The spreading of a drop by capillary action, *J. Fluid Mech.* **121**, 425 (1982).
32. L. Zhornitskaya and A. L. Bertozzi, Positivity preserving numerical schemes for lubrication-type equations, *SIAM J. Numer. Anal.* **37**, 523 (2000).
33. L. Zhornitskaya, *Positivity Preserving Numerical Schemes for Lubrication-Type Equations*, Ph.D. thesis (Duke University, 1999).
34. A. L. Bertozzi, Symmetric singularity formation in lubrication-type equations for interface motion, *SIAM J. Appl. Math.* **56**, 681 (1996).
35. F. Bernis and A. Friedman, Source-type solutions to thin-film equations in higher dimensions, *J. Differential Equations* **83**, 179 (1990).
36. R. Ferreira and F. Bernis, Source-type solutions to thin-film equations in higher dimensions, *Eur. J. Appl. Math.* **8**, 507 (1997).

37. S. Betelú and J. King, Explicit solutions of a two-dimensional fourth order non-linear diffusion equation, *Math. Comp. Modeling*, to appear.
38. G. I. Barenblatt, *Scaling, Self-Similarity, and Intermediate Asymptotics* (Cambridge Univ. Press, Cambridge, UK, 1996).
39. A. Menchaca-Rocha, A. Martínez-Dávalos, R. Nuñez, S. Popinet, and S. Zaleski, Coalescence of liquid drops by surface tension, *Phys. Rev. E* **63**, 046309 (2001).
40. C. Andrieu, D. A. Beysens, V. S. Nikolaev, and Y. Pomeau, *J. Fluid. Mech.* **453**, 427 (2002).
41. L. Tanner, The spreading of silicone oil drops on horizontal surfaces, *J. Phys. D.* **12**, 1473 (1979).
42. Animations can be found at http://math.njit.edu/~kondic/thin_films/drops.html.